

Individual variability and connectivity dynamics in modular organization of human cortical functional networks

Makoto Fukushima^{1,*}, Richard F. Betzel^{1,2}, Ye He^{1,3}, Marcel A. de Reus⁴, Martijn P. van den Heuvel⁴, Xi-Nian Zuo³, Olaf Sporns^{1,5}

¹Department of Psychological and Brain Sciences, Indiana University, Bloomington, Indiana 47405

²Department of Bioengineering, University of Pennsylvania, Philadelphia, Pennsylvania 19104

³Key Laboratory of Behavioral Science and Magnetic Resonance Imaging Research Center, Institute of Psychology, Chinese Academy of Sciences, Beijing, China

⁴Department of Psychiatry, Brain Center Rudolf Magnus, University Medical Center Utrecht, Utrecht, The Netherlands

⁵Indiana University Network Science Institute, Bloomington, Indiana 47405

***Corresponding author:**

Makoto Fukushima

Department of Psychological and Brain Sciences,

Indiana University,

1101 East 10th Street,

Bloomington, Indiana 47405

Email: mfukushi @ indiana.edu

Abstract

There is growing evidence for modules in structural networks of neural populations and brain regions. Modular organization is extensively observed in functional networks as well, where connectivity in networks is quantified based on statistical dependencies between neuronal or regional time series. Studies of such functional networks derived from human functional magnetic resonance imaging have shown individual variability in modularity. In parallel, recent studies reported that functional networks during resting state vary on a time scale of tens of seconds. However, little is known about fluctuations of modularity in time-varying functional networks, as well as their relation to individual variations in modularity measured over longer time scales. Here, we relate individual variations and dynamic fluctuations in the modularity of functional cortical networks and investigate connectivity patterns in networks during periods of high and low time-resolved modularity. After confirming that individual differences in

long-time-scale modularity persisted across multiple resting-state sessions, we showed that time-resolved functional connectivity displayed highly modular connectivity patterns more frequently in subjects exhibiting high long-time-scale modularity. Compared to the low modularity periods, time-resolved functional connectivity patterns during the high modularity periods exhibited greater similarity to each other, where the patterns were characterized by pronounced dissociation of the default mode network from the attention and primary sensory networks. The functional connectivity patterns averaged within periods of high/low modularity exhibited lower/higher similarity to connectivity patterns observed in structural networks, respectively, indicating that characteristic connectivity features observed during the high modular state were associated with a shift away from the underlying structural connectivity. Taken together, these results suggest that individual variations in long-time-scale modularity can be traced to individual variations in ongoing fluctuations of short-time-scale modularity, which can be characterized by the recurrence of increased default mode network segregation and significant divergence from structural connectivity patterns.

Keywords: Connectomics, Functional connectivity dynamics, Modularity, Networks, Resting state

1. Introduction

Neural populations and brain regions form networks linked by structural connections (White et al., 1986; Felleman and Van Essen, 1991; Scannell et al., 1995; Hagmann et al., 2007). In such structural networks, there is growing evidence for modules, defined as subnetworks of densely interconnected populations or regions that are only sparsely connected with the rest of the network, in the *Caenorhabditis elegans* nerves system (Jarrell et al., 2012; Towilson et al., 2013), the cat and macaque brain (Hilgetag et al., 2000; Zamora-López et al., 2010; Harriger et al., 2012; de Reus and van den Heuvel, 2013) as well as the human brain (Hagmann et al., 2008; van den Heuvel and Sporns, 2011, 2013; for a review, see Sporns and Betzel, 2016). The modular organization of networks is known to have several advantages in function; e.g., adaptability to a changing environment (Kashtan and Alon 2005; Kashtan et al., 2007) and conservation of wiring cost (Bullmore and Sporns, 2012; Clune et al, 2013). Modular organization is also found in brain functional networks in which connectivity strength is defined based on statistical dependencies (e.g., correlation coefficient) between neuronal or regional time series (Yu et al., 2008; Meunier et al., 2009b; Power et al., 2011; Shen et al., 2012).

Modular organization of functional networks in human cerebral cortex is often derived from temporal correlations among regional blood oxygenation level dependent (BOLD) time series, estimated over several minutes of resting-state functional magnetic resonance imaging (rs-fMRI) scans (Power et al., 2011). In human cortical functional networks, previous studies reported that modularity (i.e., the degree to which modules dissociate from each other) varies across individuals and exhibits relationships with demographic measures (Meunier et al., 2009a; Betzel et al., 2014; Cao et al., 2014b; Chan et al., 2014; Geerligs et al., 2015) and behavioral performance (Bassett et al., 2011; Kitzbichler et al., 2011; Stevens et al., 2012). In parallel, recent studies have demonstrated that resting-state functional connectivity dynamically varies on a time scale of tens of seconds (Chang and Glover, 2010; Handwerker et al., 2012; Hutchison et al., 2013b; Gonzalez-Castillo et al., 2014; Zalesky et al., 2014; Shen et al., 2015; Zhang et al., 2016; for reviews, see Hutchison et al., 2013a; Calhoun et al., 2014), resulting in dynamic changes of connectivity patterns in functional networks (Leonardi et al., 2013; Allen et al., 2014; Damaraju et al., 2014; Barttfeld et al., 2015; Chen et al., 2016) including their modular organization (Jones et al., 2012; Betzel et al., 2016).

While modular organization of functional networks was shown to vary between and within individuals, little is known about within-individual fluctuations of modularity measured over shorter time scales and their relation to between-individual variability in modularity measured over longer time scales. For instance, it is unknown how fluctuations of modularity in “time-resolved” analysis differ across individuals expressing high and low modularity in “time-averaged” analysis. For modularity fluctuations within each individual, connectivity patterns during periods of high and low modularity remain relatively unexplored. In particular, it is unclear what spatiotemporal patterns in networks are behind the ongoing modularity fluctuations and how these patterns are related to the underlying structural connectivity.

To address this gap in knowledge, we aimed to clarify relationships between individual variations and dynamic fluctuations in the modularity of functional connectivity and characterize dynamic functional connectivity patterns during high and low modularity periods. Specifically, we related long-time-scale modularity to metrics representing fluctuations of short-time-scale modularity across individuals and investigated time-resolved functional connectivity in each modularity state by examining its network topology referring to known intrinsic resting-state networks (Yeo et al., 2011) and its similarity among transient connectivity patterns as well as to structural connectivity. Reproducibility of our findings was assessed using two public datasets employing different methodologies for cortical parcellation and time-resolved functional connectivity. Test-retest reliability of modularity measures in time-averaged and time-resolved analyses was evaluated using multisession rs-fMRI data.

2. Materials and Methods

2.1. Data sets

Two publicly available imaging datasets were used in this study. The first dataset comes from Release 1–5 of the enhanced Nathan Kline Institute-Rockland Sample (NKI-RS; http://fcon_1000.projects.nitrc.org/indi/enhanced). The data were collected with the approval of the institutional review board and all subjects provided written informed consent (Nooner et al., 2012). The original number of subjects in this dataset was 418 across the lifespan. Using exactly the same procedure as in Betzel et al. (2016), we extracted a quality controlled sub-sample of healthy adults aged ≥ 18 years and ≤ 30 years, comprising 80 participants (42 males). Within this sample, diffusion MRI (dMRI) data were available in 73 individuals (37 males). Imaging data were acquired with a 32-channel head coil on a 3T Siemens Tim Trio scanner. We utilized rs-fMRI data with the shortest repetition time (TR) of 645 ms in the NKI dataset because fast sampling of rs-fMRI volumes is advantageous when focusing on connectivity dynamics. The rs-fMRI data were collected in a single run of about 10 min (900 time points) in an eyes open condition with the following scanning parameters: echo time (TE) = 30 ms, flip angle = 60° , voxel size = 3 mm isotropic, field of view (FOV) = $222 \times 222 \text{ mm}^2$, and 40 slices. Scanning parameters of dMRI data were TR = 2400 ms, TE = 85 ms, flip angle = 90° , voxel size = 2 mm isotropic, FOV = $212 \times 212 \text{ mm}^2$, and 64 slices. The total number of dMRI volumes was 137, which included 128 volumes with an effective mean b -value of 1500 s/mm^2 with different gradient directions and 9 interleaved low diffusion volumes (b_0 images) with a b -value of 5 s/mm^2 with the same gradient direction. A T1-weighted structural image was collected with TR = 1900 ms, TE = 2.52 ms, flip angle = 9° , voxel size = 1 mm isotropic, FOV = $250 \times 250 \text{ mm}^2$, and 176 slices.

The second dataset comes from the Washington University-University of Minnesota (WU-Minn) consortium of the Human Connectome Project (HCP; <http://www.humanconnectome.org>). Participants were recruited by the WU-Minn HCP consortium and all subjects provided written informed consent (Van Essen et al., 2013). We focused on the sample labeled “100 Unrelated Subjects” in the database of HCP (ConnectomeDB, <https://db.humanconnectome.org>). There were 15 participants excluded because of their head movement during rs-fMRI scans, which met at least one of the following criteria in any of runs: (1) maximum translation $> 3 \text{ mm}$, (2) maximum rotation $> 3^\circ$, or (3) mean framewise displacement $> 0.2 \text{ mm}$ (Xu et al., 2015; Betzel et al., 2016), where framewise displacement was computed using the l_2 norm of the six translation and rotation parameter differences in motion correction. We eliminated in addition one participant aged ≥ 36 years and finally obtained a sample of healthy adults aged ≥ 22 years and < 36

years, comprising 84 individuals (40 males). Imaging data were acquired using a modified 3T Siemens Skyra scanner with a 32-channel head coil. Resting-state fMRI data in an eyes open condition were collected in four runs of approximately 15 min (1200 time points) each, two runs in one session at day 1 and two runs in another session at day 2 (scanning parameters: TR = 720 ms, TE = 33.1 ms, flip angle = 52°, voxel size = 2 mm isotropic, FOV = 208 × 180 mm², and 72 slices). In each session, the data were acquired with opposing phase encoding directions, left-to-right (LR) in one run and right-to-left (RL) in the other run. Diffusion MRI data were acquired with 270 gradient directions, three shells (b -value = 1000, 2000, 3000 s/mm²), two repeats, and in a total of 18 × 2 b_0 scans (TR = 5520 ms, TE = 89.5 ms, flip angle = 78°, voxel size = 1.25 mm isotropic, FOV = 210 × 180 mm², and 111 slices). Scanning parameters of a T1-weighted structural image was TR = 2400 ms, TE = 2.14 ms, flip angle = 8°, voxel size = 0.7 mm isotropic, FOV = 224 × 224 mm², and 320 slices.

2.2. Image preprocessing

The acquired images in the NKI dataset were preprocessed using the Connectome Computation System pipeline (CCS; <https://github.com/zuoxinian/CCS>) (Xu et al., 2015), which incorporates functions included in standard neuroimaging software: AFNI (Cox, 2012), Diffusion Toolkit (Wang et al., 2007), Freesurfer (Fischl, 2012), FSL (Jenkinson et al., 2012), and SPM (Ashburner, 2012). The preprocessing steps of rs-fMRI data included (1) discarding the first volumes of 10 s, (2) removing and interpolating temporal spikes, (3) slice timing and motion correction, (4) 4D global mean intensity normalization, (5) co-registration between individual functional and structural images, (6) regressing out global, white matter, and cerebrospinal fluid mean signals and the Friston-24 motion time series (Friston et al., 1996), (7) temporal band-pass filtering (0.01–0.1 Hz), (8) removal of linear and quadratic trends, and (9) projection of the preprocessed 4D time series onto standard volumetric (MNI152) and cortical surface (fsaverage5) spaces. Temporal spikes were removed and interpolated using the function “3dDespike” in AFNI, where the spikes were determined based on signal deviations in the BOLD signal. Correlation coefficient between the number of interpolated voxels and mean framewise displacement was low ($r = 0.08$). The dMRI preprocessing included (1) correction for eddy current distortions, (2) realignment of all images to the mean of b_0 images, (3) diffusion tensor fitting at each voxel, (4) computation of fractional anisotropy in each voxel, (5) deterministic streamline tracking using the FACT algorithm (Mori et al., 1999), and (6) co-registration between diffusion and structural images.

For the HCP dataset, we used images in ConnectomeDB preprocessed with the minimal preprocessing pipelines adopted by the HCP (Glasser et al., 2013). The minimal preprocessing for rs-fMRI data included (1) gradient distortion correction, (2) motion correction, (3) bias field removal, (4) spatial distortion correction, (5) transformation to MNI space, and (6) intensity normalization. The pipelines for dMRI data included (1) intensity normalization, (2) spatial distortion correction, (3) eddy current and motion correction, (4) gradient nonlinearly correction, and (5) transformation to MNI space. The rs-fMRI data were further preprocessed in the following order: (1) discarding the first 10 s volumes, (2) despiking and interpolating time series using 3dDespike [correlation coefficient between the number of interpolated voxels and mean framewise displacement; session 1–phase LR (run 1LR), 0.30; 1RL, 0.15; 2LR, 3.5×10^{-3} ; 2RL, 0.26], (3) regressing out global, white matter, and cerebrospinal fluid mean signals and the Friston-24 motion time series, (4) temporal band-pass filtering [cutoff: low, $1/(66 \text{ TRs})$ Hz; high, 0.1 Hz], and (5) linear and quadratic detrending. From the preprocessed dMRI data, white matter fibers were reconstructed using generalized q -sampling imaging (Yeh et al., 2010, crossing fibers can be reconstructed) and deterministic streamline tractography. Tractography procedures are detailed in de Reus and van den Heuvel (2014) and van den Heuvel et al. (2015, 2016).

2.3. Cortical parcellation

Functional and structural connectivity analyses were performed in a region-wise manner within the cortex. In the NKI dataset, we used a functional cortical parcellation defined based on the similarity of intrinsic FC profiles in 1000 subjects (Yeo et al., 2011). The whole cortex was separated into 114 regions forming a subdivision of 17 network components in the Yeo parcellation (Fig. 1A and Table 1; also see Betzel et al. 2014). One region (dorsal prefrontal cortex in the left hemisphere, numbered 84 in Fig. 1A) was discarded due to its small surface area and the remaining 113 regions were used as nodes in functional and structural networks. In the HCP dataset, the cortex was parcellated into 114 distinct regions on the basis of a subdivision of the Desikan-Killiany anatomical atlas in FreeSurfer (Fig. 1B) (Cammoun et al., 2012; subdivision can be performed using the atlas files “myatlas_60_lh.gcs” and “myatlas_60_rh.gcs” in Connectome Mapper, <https://github.com/LTS5/cmp>). Based on the area of overlap, each region in this parcellation was uniquely associated with one of the 17 network components in the Yeo parcellation. The association of regions and networks is shown in the lower right columns of Figure 1. All 114 regions were represented in at least one of the 17 networks.

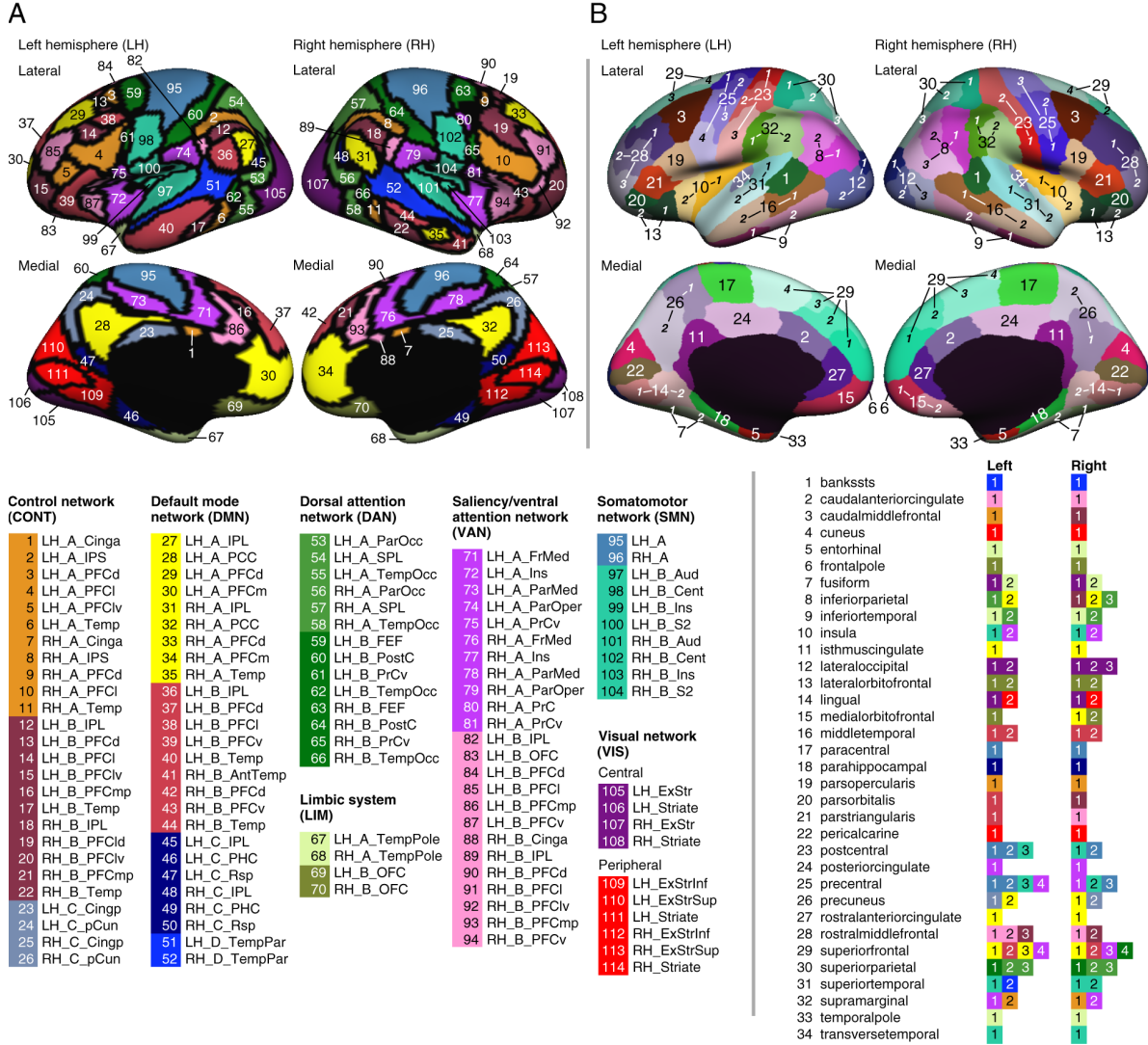


Figure 1. Cortical regions projected onto inflated left and right cortical surfaces. **A**, Cortical parcellation in the NKI dataset (a subdivision of the Yeo 17-Network parcellation). The numbers placed on the surfaces indicate the position of regions listed below the surfaces (for abbreviations, see Table 1). The order of numbers corresponds to the order of regions in functional and structural connectivity matrices in subsequent figures. **B**, Cortical parcellation in the HCP dataset. A part of the 34×2 cortical regions in the Desikan-Killiany atlas in FreeSurfer are subdivided into 2–4 subregions. The color of squares next to the region list indicates the maximally overlapped network component in the Yeo 17-Network parcellation. The labels of network components were used for sorting regions in connectivity matrices. In each network components, regions in the left hemisphere are shown first and regions in the right hemisphere second. Regions within each left/right network component were sorted alphabetically.

Table 1. Abbreviations for cortical regions in the NKI dataset.

Abbreviation	Region name
AntTemp	Anterior temporal cortex
Aud	Auditory cortex
Cent	Central sulcus
Cinga	Anterior cingulate cortex
Cingp	Posterior cingulate cortex
ExStr	Extrastriate cortex
ExStrInf	Inferior extrastriate cortex
ExStrSup	Superior extrastriate cortex
FEF	Frontal eye fields
FrMed	Medial frontal cortex
Ins	Insula
IPL	Inferior parietal lobule
IPS	Intraparietal sulcus
OFC	Orbitofrontal cortex
ParMed	Medial parietal cortex
ParOcc	Parieto-occipital cortex
ParOper	Parietal operculum
PCC	Posterior cingulate cortex
pCun	Precuneus
PFCd	Dorsal prefrontal cortex
PFCl	Lateral prefrontal cortex
PFCld	Dorsolateral prefrontal cortex
PFClv	Ventrolateral prefrontal cortex
PFCm	Medial prefrontal cortex
PFCmp	Posterior-medial prefrontal cortex
PFCv	Ventral prefrontal cortex
PHC	Parahippocampal cortex
PostC	Post-central cortex
PrC	Pre-central cortex
PrCv	Ventral pre-central cortex
Rsp	Retrosplenial cortex
S2	Secondary somatosensory cortex
SPL	Superior parietal lobule
Striate	Striate cortex
Temp	Temporal cortex
TempOcc	Temporo-occipital cortex
TempPar	Temporo-parietal cortex
TempPole	Temporal pole

2.4. Functional connectivity and window parameters

As a metric of functional connectivity, we used the Fisher z -transformed Pearson correlation coefficient between pairs of rs-fMRI time series averaged within each cortical region. In time-averaged analysis, functional connectivity was estimated with this metric computed from the total duration of rs-fMRI time series. Whereas in time-resolved analysis, time-resolved functional connectivity was estimated using a tapered sliding window approach. We used two types of tapered windows to obtain results that are not window parameter specific. In the NKI dataset, an exponential tapered window employed in Zalesky et al. (2014) was used with a window width of 100 s, a step size of 1 TR, resulting in a total number of 730 windows. In the HCP dataset, we used an approach adopted in Allen et al. (2014). Specifically, the tapered window was created by convolving a rectangle (width = 66 TRs = 47.52 s) with a Gaussian kernel ($\sigma = 9$ TRs = 6.48 s) and was moved in steps of 3 TRs = 2.16 s, resulting in a total number of 369 windows.

2.5. Structural connectivity

We quantified structural connectivity based on the number of streamlines between cortical regions. Since the size of regions has an effect on the number of streamlines (Hagmann et al., 2008), we derived its density, computed as the streamline count between regions i and j , divided by the geometric mean of the surface area of regions i and j . For purposes of comparing structural to functional networks, we rescaled the magnitude of structural connectivity strengths by resampling the streamline density into a Gaussian distribution with a mean of 0.5 and an SD of 0.1 (Honey et al., 2009), maintaining the rank order of edge weights across the raw and resampled values. When averaging connectivity strength across subjects, we set to zero all those connections for which no streamlines were found in more than half of the subjects.

2.6. Community detection and a measure of modularity

Communities in networks were identified by maximization of a modularity quality function (Newman and Girvan, 2004). Since functional networks may contain negative edge weights, the asymmetric generalization of the quality function introduced in Rubinov and Sporns (2011) as Q^* was applied throughout the paper (hereafter we denote by Q this quality function). The maximized Q was used as a measure of modularity for evaluating the degree of modularity or the “goodness” of a given partition. Since the behavior of this modularity measure Q depends both on the size of networks and the resolution of community partitions (Good et al., 2010), we compare Q only between functional networks derived from individual datasets and computed for a single default setting of the resolution parameter.

Community detection and Q computation were performed using the function “community_louvain.m” in the Brain Connectivity Toolbox (BCT version 2016-01-16; <http://www.brain-connectivity-toolbox.net>) with the default resolution parameter $\gamma=1$. We ran this function 100 times and chose the maximum Q and its corresponding community partitions. Similarity of partitions (or modules) between networks was quantified by the normalized mutual information using the BCT function “partition_distance.m.” For time-resolved functional networks, the quality function was computed separately in each window, yielding a time-resolved modularity measure Q_w for $w = 1, \dots, W$, where w is a window index and W is the number of windows.

2.7. Periods of high and low modularity

Periods of high/low modularity in time-resolved functional connectivity were defined as periods in which time-resolved modularity was significantly higher/lower than its median across subjects, respectively. To compare time-resolved connectivity patterns across individuals, we used a single set of thresholds for determining high/low modularity periods. The significance of high and low modularity was evaluated based on null distributions of fluctuations in modularity amplitude, derived from null models assuming stationarity of time-resolved functional connectivity.

Null time-resolved functional connectivity was generated using stationary vector autoregressive (VAR) models as described in Zalesky et al. (2014). Parameters in null stationary VAR models were first estimated from actual rs-fMRI time series for each pair of regions. The order of VAR models were set to 12 (NKI) and 11 (HCP) to use a maximum lag of approximately 8 s as in Zalesky et al. (2014). The VAR models with the estimated parameters were then used for individually simulating null stationary rs-fMRI time series for each pair of regions (initial values for simulation: a randomly-sampled contiguous block of actual rs-fMRI time series; the innovation term: a randomly-sampled residual of the VAR estimation). Finally, from the simulated rs-fMRI data, the null time-resolved functional connectivity was computed in the same way as the actual data. As in Zalesky et al. (2014), a total of approximately 2500 null samples were generated from actual data of all subjects for each run (NKI, 32 samples \times 80 subjects; HCP, 30 samples \times 84 subjects) (Fig. 2A).

Null distributions of fluctuations in modularity amplitude were obtained from the modularity time series of null time-resolved functional connectivity (Fig. 2B). A threshold with $\alpha = 0.01$ was used for testing whether time-resolved modularity fluctuates significantly more than expected by chance. Figure 2C shows the way of determining periods of

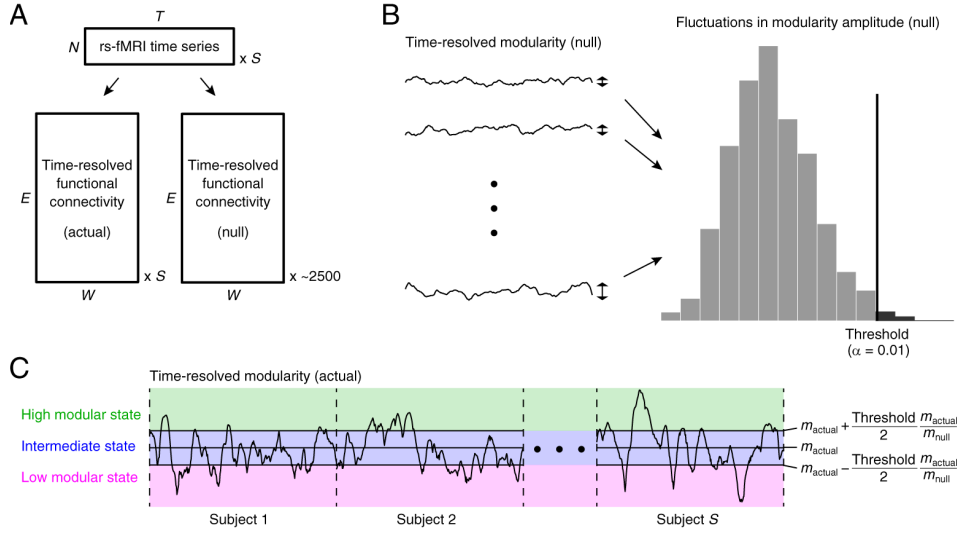


Figure 2. Workflow diagram. **A**, Schematic view of the computation of actual and null time-resolved functional connectivity. N : Number of regions; T : Number of time samples; E : Number of connections; W : Number of windows; S : Number of subjects. **B**, Modularity time series of null time-resolved functional connectivity (left) and null distributions of fluctuations in modularity amplitude (right). The threshold with $\alpha = 0.01$ was used for determining periods when time-resolved modularity was higher or lower than expected by chance. **C**, Modularity time series of actual time-resolved functional connectivity. Based on the threshold specified in **B** and the median of time-resolved modularity, state labels (high modular/intermediate/low modular) are assigned to each window. m_{actual} : median of actual time-resolved modularity across all subjects; m_{null} : median of null time-resolved modularity across all null samples.

high and low modularity using this threshold. The “high modular state” was defined as periods in which time-resolved modularity was larger than $m_{\text{actual}} + (\text{threshold} / 2) \times (m_{\text{actual}} / m_{\text{null}})$, where m_{actual} and m_{null} are the median of actual and null time-resolved modularity across all samples, respectively, and the threshold was multiplied with $m_{\text{actual}} / m_{\text{null}}$ for normalization. Similarly, the “low modular state” was defined as periods when time-resolved modularity was less than $m_{\text{actual}} - (\text{threshold} / 2) \times (m_{\text{actual}} / m_{\text{null}})$, and the “intermediate state” as periods other than the high and low modular states. Note that generating null data by phase randomizing (Prichard and Theiler, 1994) the regional time series is not appropriate for defining the states since phase randomization does not necessarily ensure stationarity of the time series of time-resolved functional connectivity (see supplemental information in Zalesky et al., 2014).

2.8. Metrics for state representation

States derived from time-resolved functional connectivity were assessed using frequency, mean dwell time, and transition probability (Allen et al., 2014; Damaraju et al., 2014; Hutchison and Morton, 2015). Frequency is defined

as the ratio of the number of windows classified into a particular state relative to the total number of windows. Mean dwell time is the number of consecutive windows classified into a particular state, averaged within each subject. We set to zero the mean dwell time of a state to which no windows were assigned. We omitted the first and last segments of consecutive windows in a subject’s time series from the mean dwell time since the beginnings and end of these episodes fall outside of the scanning period. We did not define the mean dwell time of a state in a subject when all its consecutive windows overlapped with either the start or end windows. The transition probability is measured as the averaged proportion of states in the window immediately following a given window with a particular state. We did not define the transition probability from a state to another in a subject if no windows were classified into the corresponding state.

2.9. Test-retest analysis

Test-retest reliability of modularity measures in time-averaged and time-resolved analyses was evaluated using the intra-class correlation coefficient (ICC; Shrout and Fleiss, 1979). ICC has been used in a number of test-retest studies on rs-fMRI data (Schwarz and McGonigle, 2011; Wang et al., 2011; Braun et al., 2012; Guo et al., 2012; Cao et al., 2014a; Zuo and Xing, 2014; Andellini et al., 2015). Using the multisession rs-fMRI data in the HCP dataset, we assessed across-run consistency of Q , $\frac{1}{W} \sum_{w=1}^W Q_w$, frequency and mean dwell time by computing ICC under a two-way mixed model (McGraw and Wong, 1996): $(BMS - EMS) / (BMS + (l-1)EMS)$, where BMS is the between-subjects mean square, EMS is the error mean square, and l is the number of repeated runs per subject. According to previous rs-fMRI test-retest studies (Guo et al., 2012; Andellini et al., 2015), we interpreted $0.2 < ICC \leq 0.4$ as indicative of a fair test-retest reliability and $ICC > 0.4$ as moderate to good test-retest reliability. Consistent with Braun et al. (2012), Cao et al. (2014a) and Andellini et al. (2015), negative ICC scores were set to zero, since the reason for a presence of negative ICCs is unclear (Muller and Buttner, 1994) and negative reliability is difficult to interpret (Rousson et al., 2002).

2.10. Linear regression analysis

We performed linear regression analysis to examine relations of modularity measures between time-averaged and time-resolved analyses. We used a standard linear regression model: $y_s = \beta_0 + \beta_e x_{e,s} + \boldsymbol{\beta}_n^T \mathbf{x}_{n,s} + \varepsilon_s$, for $s = 1, \dots, S$, where s is a subject index, S is the number of subjects, y_s is a target variable, $x_{e,s}$ is an explanatory variables, $\mathbf{x}_{n,s}$ is a column vector of nuisance variables, ε_s is an error term, and β_0 , β_e , and $\boldsymbol{\beta}_n$ are regression parameters to the constant

term, explanatory variable, and nuisance variables, respectively. In our analysis, Q was used as an explanatory variable and $\frac{1}{W} \sum_{w=1}^W Q_w$, frequency, or mean dwell time was used as a target variable. Gender, total intracranial volume, mean framewise displacement and linear and quadratic terms of age were used as nuisance variables. In the HCP dataset, the middle years in each age category, 24, 28.5, and 33.5 years, were used instead of the exact subject ages since they are not part of the open data release. A one-sample t -test was performed on the regression parameter β_e to assess the significance of the linear relationship.

2.11. Principal component analysis

To visualize trajectories of time-resolved functional connectivity and modularity state transitions in a two dimensional space, we applied principal component analysis to the time series of functional connectivity (Leonardi et al., 2013). According to the approach taken by Leonardi et al., principal components were obtained by eigenvalue decomposition: $\mathbf{CC}^T = \mathbf{UDU}^T$. \mathbf{C} is a matrix of time-resolved functional connectivity concatenated across subjects (an $E \times WS$ matrix), where temporal average of time-resolved connectivity in each subject (an $E \times 1$ vector) was subtracted individually. \mathbf{U} is a matrix containing the eigenvectors of \mathbf{CC}^T (i.e., the principal components of \mathbf{C}) in its columns and \mathbf{D} is a diagonal matrix containing the corresponding eigenvalues. The weights of principal components were derived as $\mathbf{U}^T \mathbf{C}$, representing the contribution of each principal component in the variability of time-resolved functional connectivity over time. Trajectories of time-resolved functional connectivity were visualized by plotting the weights of the first and second principal components and modularity state transitions were represented by embedding state metrics into this two dimensional principal component space.

2.12. k -means clustering

We compared the states determined based on modularity to states derived from k -means clustering, which has been used for detecting a small set of brief functional connectivity patterns in previous studies (Allen et al., 2014; Damaraju et al., 2014; Barttfeld et al., 2015; Hutchison and Morton, 2015; Gonzalez-Castillo et al., 2015). The k -means clustering was performed using the same procedure as in Allen et al. (2014) and Barttfeld et al. (2015). In this procedure, time-resolved functional connectivity concatenated across subjects ($E \times WS$) was subsampled along the time dimension before clustering of all time window data. The subsampling was performed by choosing local maxima of the time series of functional connectivity variance, resulting in 24–41 (NKI) and 15–35 (HCP) windows per subjects in subject exemplars. The clustering algorithm was first applied to this set of subject exemplars 500 times

with the $l1$ distance metric and random initialization, and then the obtained median centroids with the minimum error were used as an initial starting point for the subsequent k -means clustering of all time window data. We varied the number of clusters k from two to ten and investigated how the states derived from k -means clustering were expressed in each modularity-based state.

3. Results

3.1. Individual variability in modularity

Figure 3A shows functional connectivity derived from time-averaged analysis. Both in the NKI and HCP datasets, functional connectivity matrices averaged across subjects exhibited, on average, positive block-diagonal correlations, positive off-diagonal correlations in DAN–VIS, VAN–SMN, and SMN–VIS (peripheral) and negative off-diagonal correlations in DMN–DAN/VAN/VIS (see Fig. 1A for abbreviations). While such canonical connectivity patterns were found in the averaged functional connectivity, connectivity patterns differ across subjects, resulting in individual variations in the spatial patterns of connections (Fig. 3A) and the modularity measure Q (interquartile range of Q distributions: NKI, 0.067; HCP-1LR, 0.079; 1RL, 0.062; 2LR, 0.047, 2RL, 0.050) (Fig. 3B).

Individual variability in the modularity Q exhibited moderate test-retest reliability (Fig. 3C). The ICC of Q across all four runs in the HCP dataset was 0.45 and its 95% confidence interval (CI) was 0.33–0.56. In addition to computing Q by optimizing partitions in each subject, we also computed Q in each subject given a fixed 7-network partition (CONT, DMN, DAN, LIM, VAN, SMN, and VIS) derived from earlier work (Yeo et al., 2011). This approach also yielded a moderate to good test-retest reliability [ICC (95% CI) among all four runs: 0.60 (0.50–0.70)]. Detected modules were similar across runs in each subject. The mutual information of partitions among all combinations of runs (mean \pm SD, 0.44 ± 0.12 ; number of modules, 2–4) was significantly greater than expected by chance (at the 99th percentile of null distributions made by randomly permuting module labels, 0.064 across all comparisons; 2500 null samples generated in each comparison). Mutual information of partitions was only weakly correlated with differences in Q ($r = -0.11$, $p = 0.012$), but appeared more strongly correlated with the magnitude of Q averaged over two runs ($r = 0.36$, $p = 5.2 \times 10^{-17}$).

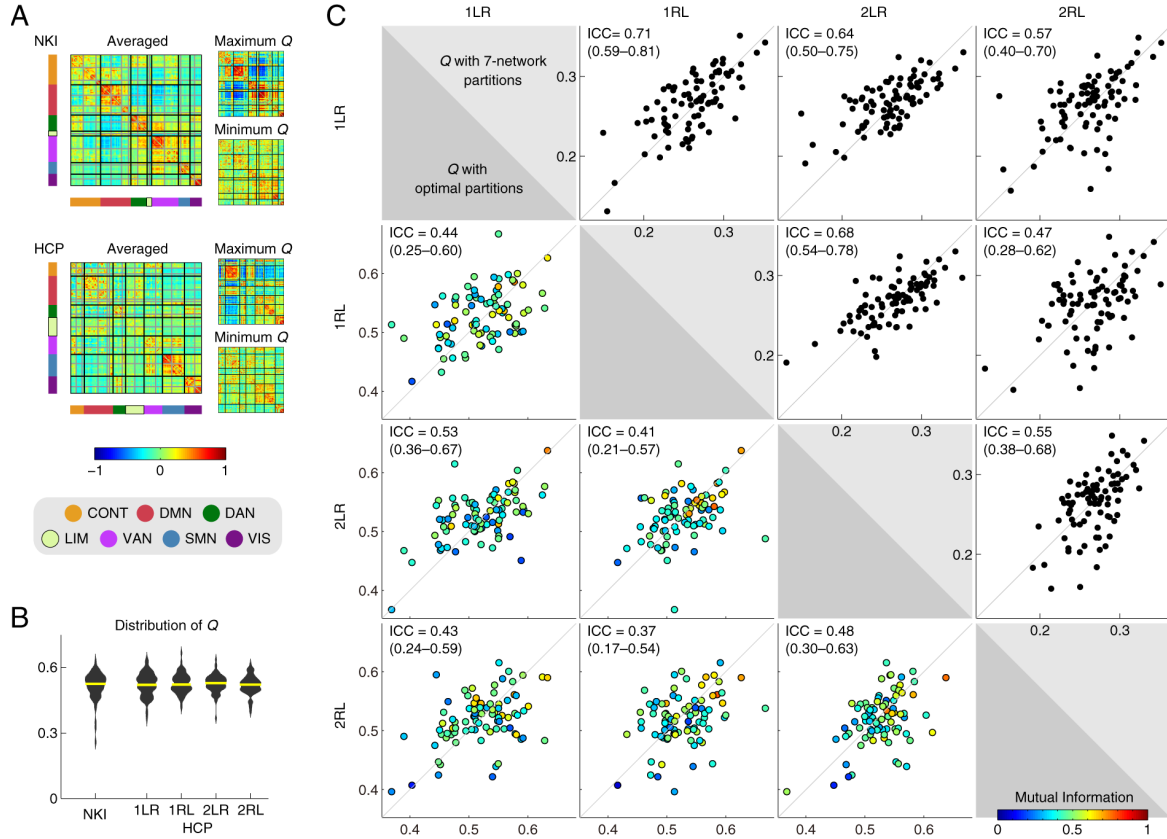


Figure 3. Time-averaged analysis of modularity in functional networks. **A**, Functional connectivity in time-averaged analysis. A connectivity matrix averaged across subjects (as well as runs) and matrices with maximum and minimum modularity Q are shown for each dataset. See caption of Figure 1 for the order of rows and columns in a connectivity matrix. **B**, Distribution of modularity Q over subjects in time-averaged analysis. A yellow line indicates the median of distribution. **C**, Scatter plots of modularity Q between different runs in the HCP dataset. ICC was shown at the top left of each scatter plot with its 95% CI. The lower triangular six scatter plots are for Q with partitions optimized by the modularity maximization (the default setting of Q computation in this paper) and the upper triangular part is for Q with the fixed 7-network partitions. The inner color of circles in the lower triangular scatter plots indicates mutual information of partitions between different runs.

Head movement is a potential confound for the detection of modules in functional networks (Power et al., 2012). In the NKI dataset, modularity Q was not significantly correlated with mean framewise displacement ($r = -0.10$, $p = 0.36$). In the HCP dataset, significant correlations with mean framewise displacement were observed in two of the four runs (1LR: $r = -0.27$, $p = 0.014$; 1RL: $r = -0.18$, $p = 0.11$; 2LR: $r = -0.10$, $p = 0.37$; 2RL: $r = -0.36$, $p = 8.4 \times 10^{-4}$; the least motion affected run was 2LR) although these correlations were relatively weak.

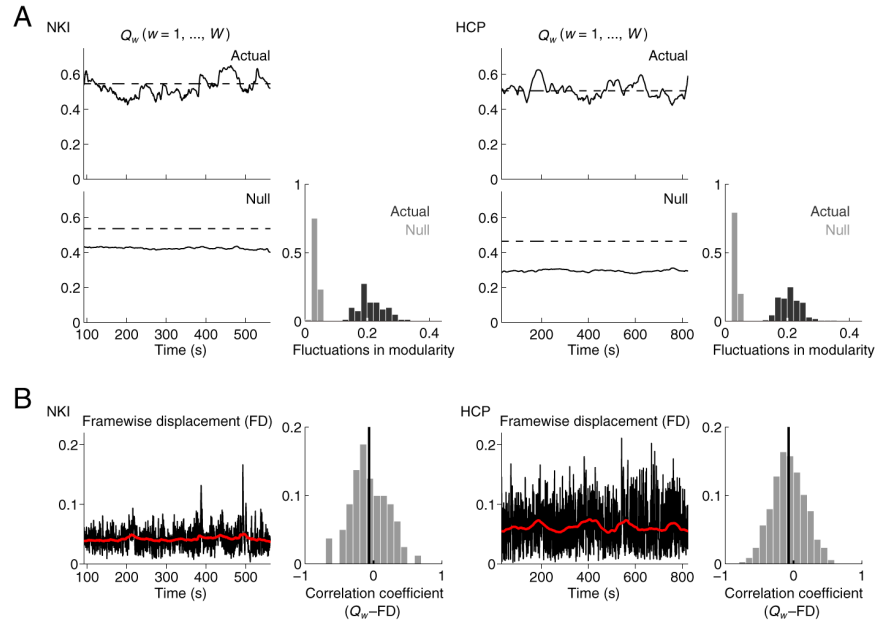


Figure 4. Time-resolved modularity. **A**, Modularity time series Q_w ($w = 1, \dots, W$) in actual and null time-resolved functional connectivity are plotted for representative subjects (subject ID 0117902 in NKI and 133928 in HCP [run 2LR]). A broken line indicates modularity in time-averaged analysis. Histograms show distributions of fluctuations in modularity amplitude in actual and null data (distributions for the HCP dataset were shown across four runs). **B**, Framewise displacement and its sliding window average (black and red time courses, respectively) in the same subjects shown in **A**. Histograms show distributions of the correlation coefficient between modularity time series and sliding window average of framewise displacement. The vertical line near zero indicates the mean of correlation distributions.

3.2. Dynamic fluctuations of modularity

Time-resolved modularity Q_w ($w = 1, \dots, W$) varied in time with a median amplitude of 0.21 in both datasets. Fluctuations in modularity amplitude were larger than the fluctuations found in the stationary null models (Fig. 4A). High and low modular states appeared in most of the subjects in both datasets. The number of subjects that did not express the high modular state was 4 (NKI; 80 subjects) and 1, 3, 1, 3 (HCP-1LR, 1RL, 2LR, 2RL; 84 subjects each), while the number of subjects that did not express the low modular state was 4 (NKI) and 0, 1, 0, 1 (HCP-1LR, 1RL, 2LR, 2RL). Modularity fluctuations were not consistently correlated with the magnitude of subject motion (Fig. 4B). On average, the correlation between the time-resolved modularity and the sliding window average of framewise displacement exhibited was found to be very weak (NKI, -0.064 ; HCP, -0.072), and remained very weak when adding a time lag between these two time series [for time lags between -30 s and 30 s, the subject-averaged correlations ranged -0.047 to -0.067 (NKI) and -0.057 to -0.074 (HCP)].

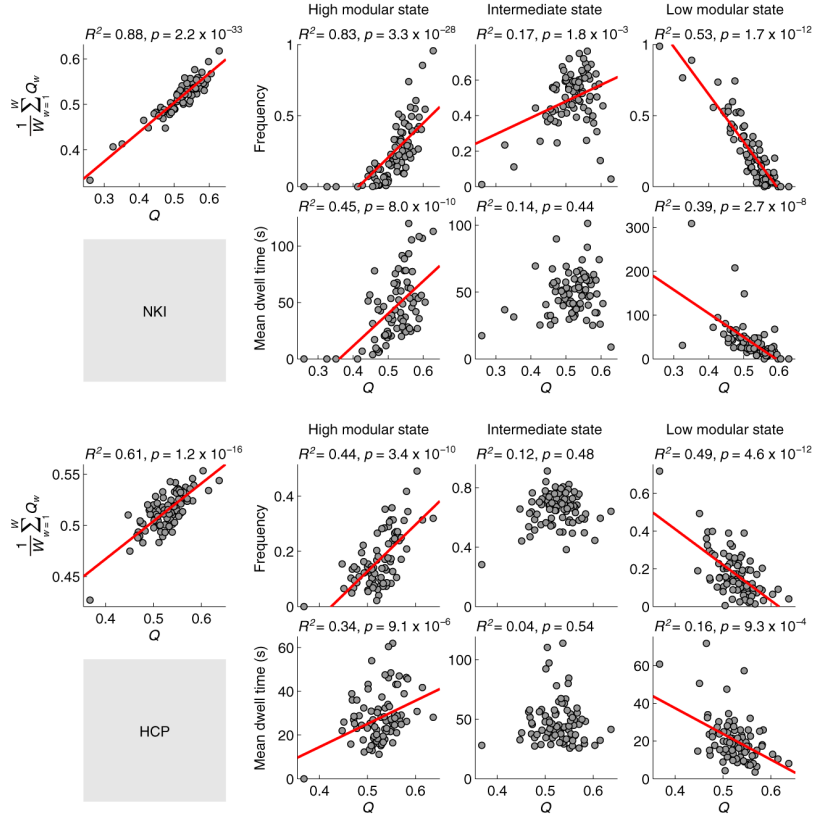


Figure 5. Relationships of modularity measures between time-averaged and time-resolved analyses (NKI and HCP [run 2LR: the least motion affected run]). Scatter plots of modularity Q in time-averaged analysis and mean time-varying modularity $\frac{1}{W} \sum_{w=1}^W Q_w$ are shown in the leftmost panel. In the other panels, scatter plots of Q and frequency (upper panels) or mean dwell time (lower panels) are shown for each modularity-based state and each dataset. The red linear fitting lines are presented in each panel if $p < 0.01$. Similar scatter plots and significance levels were obtained across all runs in the HCP dataset.

3.3. Interrelations of individual variability and modularity fluctuations

Figure 5 shows relationships of modularity measures between time-averaged and time-resolved analyses. In both datasets, the modularity Q in time-averaged analysis was positively correlated with the mean time-resolved modularity $\frac{1}{W} \sum_{w=1}^W Q_w$ as well as the frequency and mean dwell time of the high modular state, and was negatively correlated with the frequency and mean dwell time of the low modular state (R^2 and p from the linear regression analysis are shown in Fig. 5). Test-retest reliability of modularity measures in the time-resolved analysis was moderate for $\frac{1}{W} \sum_{w=1}^W Q_w$ and for the frequency of the low modular state and was fair for the frequency of the high modular state and mean dwell time of the low modular state (Table 2). These observations indicate that, in high/low modular subjects as specified from time-averaged analysis, time-resolved modularity is also high/low on average and

Table 2. Test-retest reliability of modularity measures in time-resolved analysis (bold, ICC > 0.4; bold italic, 0.2 < ICC ≤ 0.4).

HCP run		$\frac{1}{W} \sum_{w=1}^W Q_w$	High modular state		Intermediate state		Low modular state	
			Frequency	Dwell time	Frequency	Dwell time	Frequency	Dwell time
Same session, different phase encoding								
1LR–1RL	ICC	0.41	0.25	0.08	0.20	0.09	0.49	0.27
	95% CI	0.22–0.58	0.04–0.44	0–0.29	0–0.39	0–0.30	0.31–0.64	0.06–0.46
2LR–2RL	ICC	0.48	0.34	0.01	0.33	0.14	0.47	0.33
	95% CI	0.30–0.63	0.13–0.51	0–0.23	0.12–0.50	0–0.34	0.29–0.62	0.13–0.51
Different session, same phase encoding								
1LR–2LR	ICC	0.45	0.34	0.03	0.30	0	0.47	0.42
	95% CI	0.27–0.61	0.14–0.52	0–0.24	0.09–0.48	0–0.14	0.29–0.62	0.23–0.58
1RL–2RL	ICC	0.32	0.24	0.08	0	0	0.27	0.09
	95% CI	0.11–0.50	0.02–0.43	0–0.29	0–0.21	0–0.19	0.06–0.46	0–0.30
Different session, different phase encoding								
1LR–2RL	ICC	0.54	0.33	0.30	0.10	0	0.50	0.49
	95% CI	0.37–0.68	0.12–0.50	0.09–0.48	0–0.31	0–0.07	0.33–0.65	0.31–0.64
1RL–2LR	ICC	0.25	0.21	0.01	0.08	0	0.22	0.12
	95% CI	0.04–0.44	0–0.40	0–0.22	0–0.28	0–0.15	0–0.41	0–0.33
All runs across sessions								
	ICC	0.42	0.28	0.11	0.16	0	0.42	0.31
	95% CI	0.31–0.54	0.17–0.40	0.01–0.22	0.06–0.28	0–0.08	0.30–0.53	0.20–0.44

the high/low modular state is more likely to appear, respectively, suggesting that individual variations in modularity measured over long time scales are related to individual variations in modularity over short time scales.

As in the case of modularity Q in time-averaged analysis, significant correlation with mean framewise displacement was not found in the NKI dataset for $\frac{1}{W} \sum_{w=1}^W Q_w$ as well as the frequency and mean dwell time of the high and low modular states. Significant correlations observed in the HCP dataset were $r = -0.32, p = 3.1 \times 10^{-3}$ (1LR) and $r = -0.38, p = 4.2 \times 10^{-4}$ (2RL) for $\frac{1}{W} \sum_{w=1}^W Q_w$, $r = -0.31, p = 4.0 \times 10^{-3}$ (2RL) for the frequency of the high modular state, $r = -0.23, p = 0.039$ (2RL) for the mean dwell time of the high modular state, $r = 0.32, p = 2.7 \times 10^{-3}$ (1LR), $r = 0.27, p = 0.012$ (1RL), and $r = 0.31, p = 3.7 \times 10^{-3}$ (2RL) for the frequency of the low modular state, and $r = 0.22, p = 0.043$ (1LR), $r = 0.26, p = 0.016$ (1RL), and $r = 0.25, p = 0.023$ (2RL) for the mean dwell time of the low modular state. For the run 2LR, no significant correlation was observed in all measures.

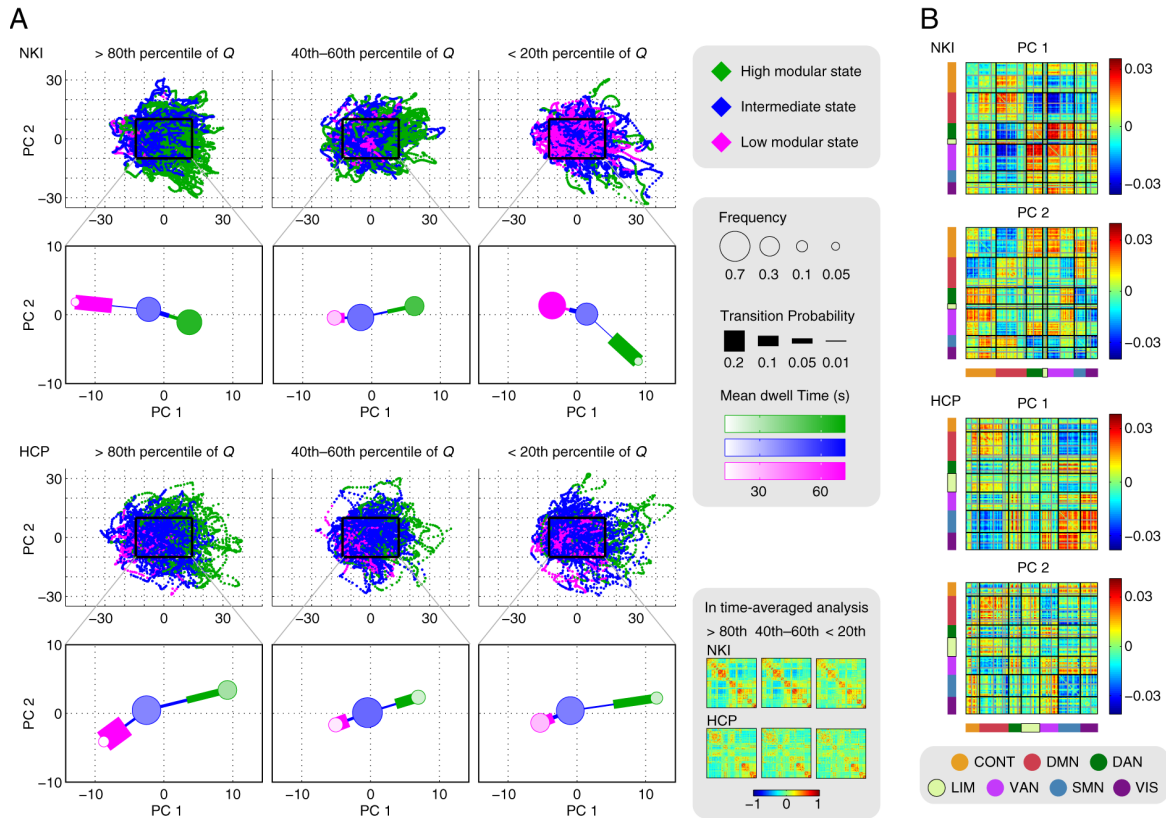


Figure 6. Principal component analysis (NKI and HCP [run 2LR]). **A**, Upper panels in each dataset: trajectories of time-resolved functional connectivity projected into a two dimensional space spanned by the first and second principal components, PC 1 and PC 2. Trajectories are separately displayed in high, middle, and low modular subjects (see text in **Results** for definition) in time-averaged analysis. Each dot represents time-resolved functional connectivity at a given time window and its color indicates the assigned state label. Lower panels in each dataset: state metrics averaged within each subject group. Frequency is shown as the area of a circle placed at the median coordinate of each state. Mean dwell time is represented by the transparency of the inner color of a circle and transition probability is expressed by the width of a line outgoing from a circle. Area of a circle and width of a line are proportional to frequency and transition probability, respectively. Linear gradation is used in a colormap for showing mean dwell time. For reference, functional connectivity in time-averaged analysis averaged within each subject group is shown in the lower right corner of this figure. **B**, Loadings of the first and second principal components. Diagrams for the HCP dataset were similar across all runs.

Heterogeneity in the dynamics of modularity across individuals can be summarized using principal component analysis. In Figure 6A, the trajectory of time-resolved functional connectivity is shown in a two dimensional space spanned by the first and second largest principal components, PC 1 and PC 2 (see Fig. 6B for loadings of these principal components). The trajectory plot is created for sets of individuals with high, middle, or low modularity Q in

time-averaged analysis (defined as subjects with Q greater than the 80th percentile, between the 40th and 60th percentiles, or less than the 20th percentile of Q distributions, respectively). Metrics for state representation (frequency, mean dwell time, and transition probability, averaged within each subject group) are presented below the trajectory plots (Fig. 6A). Results suggest that different subject groups were transitioning between states across the PC 1 axis with different transition profiles. For instance in high modular subjects, the low modular state appeared less frequently, with shorter dwell time, and greater transition probability to the intermediate state, compared to low modular subjects. Greater probability of transitioning toward the high modular state was accompanied by an increase of the PC 1 weight. The spatial pattern of PC 1 exhibits a marked dissociation of the DMN module from the DAN, VAN, SMN, and VIS modules (Fig. 6B). This suggests that greater probability of dissociation between task-negative and task-positive modules in time-resolved functional connectivity contributes to increased modularity as measured in time-averaged analysis.

3.4. Connectivity patterns during high and low modularity periods

To characterize connectivity patterns during periods of high and low modularity, we derived the median centroid of time-resolved functional connectivity in each modularity-based state (Fig. 7A). In the centroid of the high modular state, the dissociation of the DMN module from the DAN, VAN, SMN, and VIS modules was more pronounced, compared to the centroid of the low modular state. This characteristic was also found in individual time-resolved functional connectivity (Fig. 7B, connectivity matrices). We further investigated these connectivity patterns with a particular focus on similarity in connectivity and modules within each state. Similarity matrices in Figure 7B show that instances of time-resolved functional connectivity during the high modular state more strongly resemble each other, compared to the low modular state. This was found to be the case for similarity of both connectivity patterns and community partitions, measured as the correlation coefficient and mutual information, respectively. Higher similarity during periods of high modularity was observed across all runs in the NKI and HCP datasets, not only between time-resolved functional connectivity (Fig. 7C, black plots) but also between centroids and time-resolved functional connectivity (Fig. 7C, gray plots; p -values of Wilcoxon rank-sum test were essentially zero due to a large number of time windows and subjects). These findings suggest that connectivity and modules in time-resolved functional networks exhibit relatively uniform patterns during periods of high modularity; whereas the patterns are more variable and dissimilar to each other during periods of low modularity.

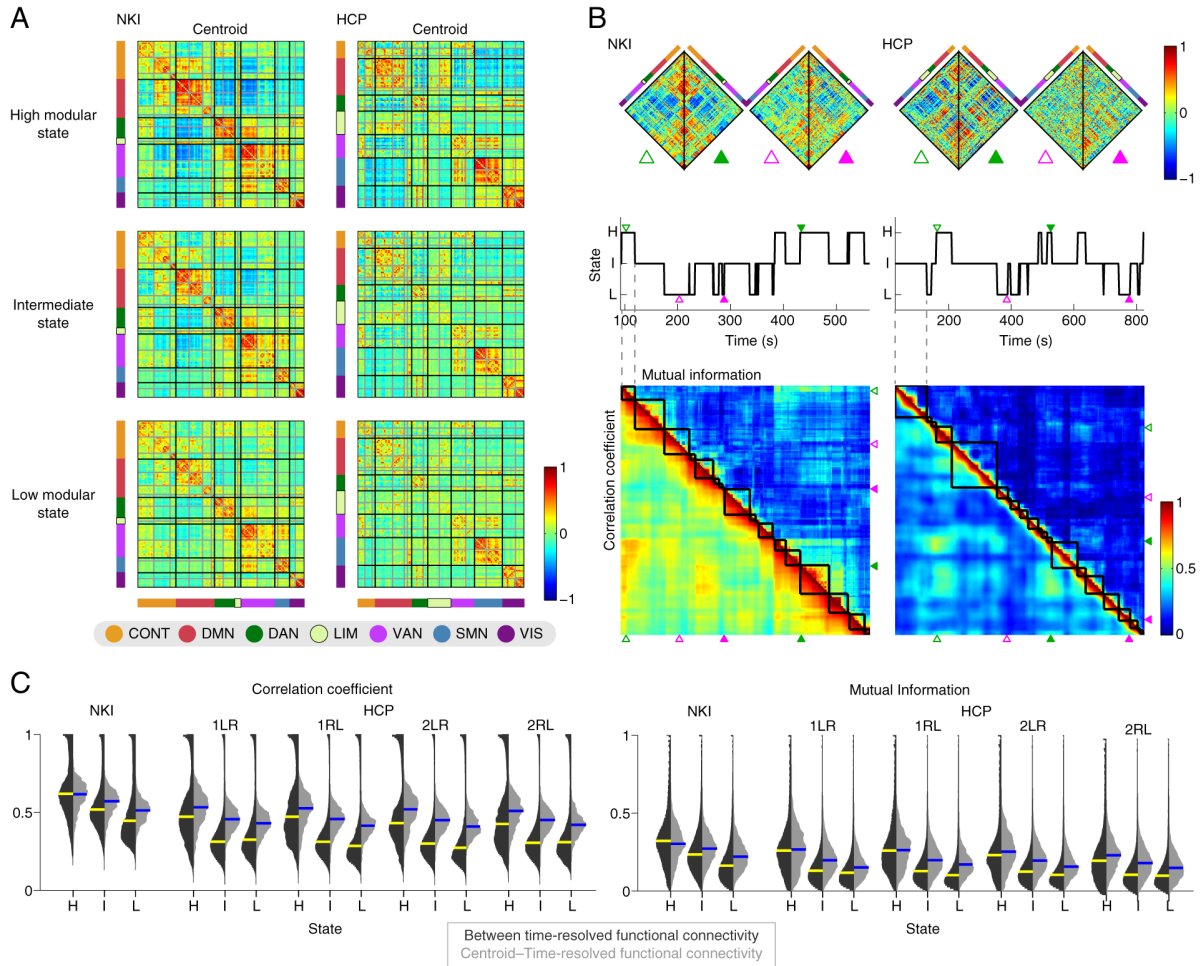


Figure 7. Connectivity patterns in each modularity-based state. **A**, Centroid of the high modular, intermediate, and low modular states (NKI and HCP [run 2LR]). The median of time-resolved functional connectivity during periods of each state is shown as a centroid. Each state centroid in the HCP dataset was quite similar across all runs (correlation coefficient of functional connectivity > 0.95). **B**, Connectivity patterns in representative subjects (the same subjects in Fig. 4). Upper: instances of time-resolved functional connectivity (green: high modular state, magenta: low modular state). Middle: sequence of state transition (H: high modular state, I: intermediate state, L: low modular state). The green and magenta triangles indicate the time points of the time-resolved functional connectivity shown in the Upper figure. Lower: similarity of connectivity and modules. Correlation coefficient between time-resolved functional connectivity is shown in the lower-triangular part and mutual information of partitions between time-resolved functional connectivity is shown in the upper-triangular part. **C**, Black distribution plots: correlation coefficient (left) and mutual information of partitions (right) between time-resolved functional connectivity during periods of each state in each individual. Yellow lines indicate the median of each distribution. Gray distribution plots: correlation coefficient (left) and mutual information of partitions (right) between time-resolved functional connectivity and its corresponding state centroid. Blue lines indicate the median of each distribution.

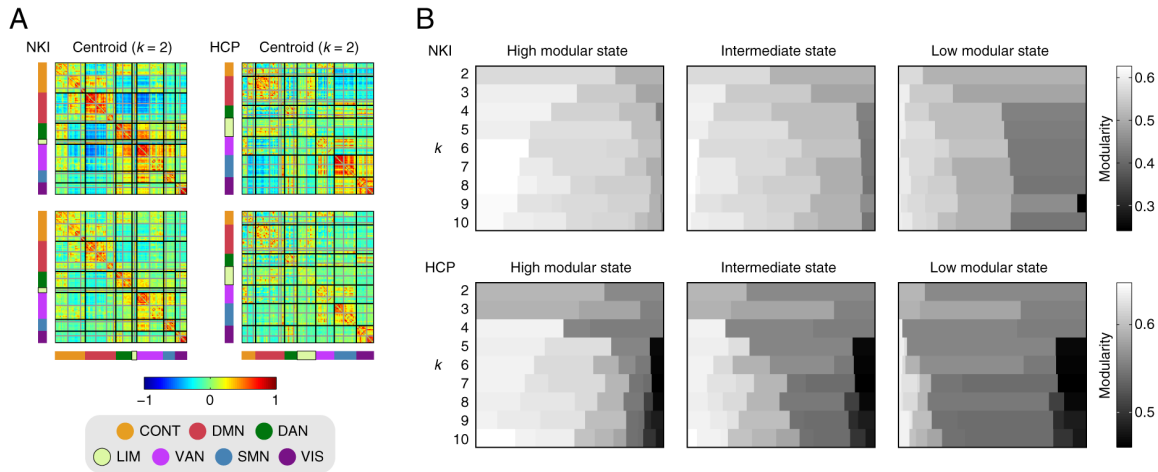


Figure 8. Relation to k -means clustering (NKI and HCP [run 2LR]). **A**, Centroid of k -means clustering with $k = 2$. The upper centroid has a higher modularity value. **B**, Ratio of states derived from k -means clustering in each modularity-based state. Cluster centroids ($k = 2, \dots, 10$) were represented using their strength of modularity. Similar diagrams were obtained across all runs in the HCP dataset.

Connectivity patterns similar to the high and low modular centroids were also observed in the median centroids of states derived from k -means clustering with $k = 2$ (Fig. 8A). During periods of the high/low modular state, cluster centroids with higher/lower modularity were more frequently detected, respectively. This characteristic was consistently observed across $k = 2, \dots, 10$ (Fig. 8B), suggesting that high and low modular durations can also be detected by a standard clustering approach with a variable number of clusters, as pursued in previous work (Allen et al., 2014).

3.5. Relation of functional patterns to structural connectivity

Finally, we compared functional connectivity patterns during periods of high and low modularity with the patterns observed in structural connectivity. Figure 9A shows resampled structural connectivity averaged across subjects. Even though there was a substantial difference in density of structural networks between the two datasets (NKI, $381 / {}_{113}C_2 = 0.060$; HCP, $1044 / {}_{114}C_2 = 0.162$), common profiles in similarity to structural connectivity were obtained from these datasets (Fig. 9B, upper plots). The high modular state centroid exhibited the lowest and the low modular state centroid the highest similarity to structural connectivity. This holds even when the similarity was assessed only within structurally-connected pairs of regions. Likewise, except for the run 2RL in the HCP dataset, modules in the high modular state centroid were the most dissimilar to modules in structural connectivity (Fig. 9B, lower plots).

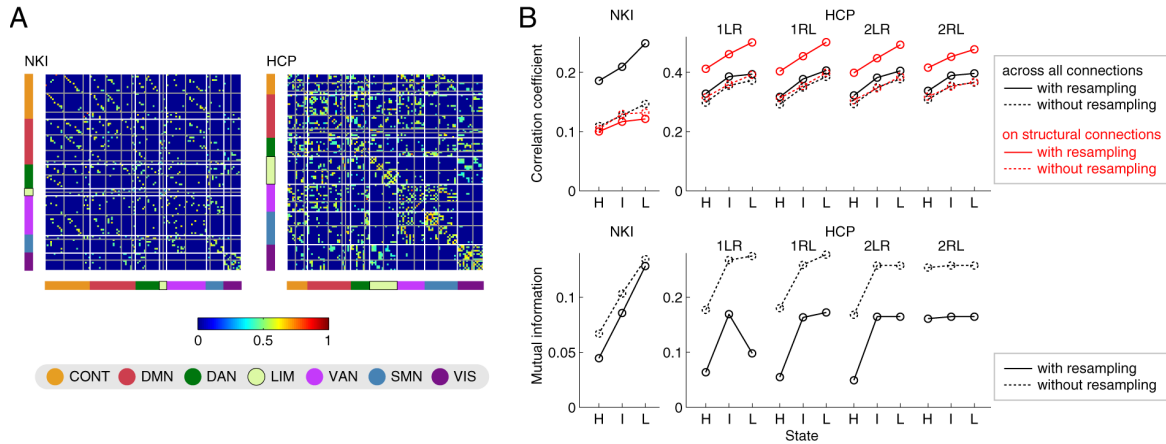


Figure 9. Relation to structural connectivity. **A**, Resampled structural connectivity averaged across subjects (NKI and HCP). Resampled strengths at structural connections were highly correlated with logarithm of strengths without resampling ($r = 0.97$ in both datasets). **B**, Upper plots: correlation coefficient between averaged structural connectivity and state centroids (H: High modular state, I: Intermediate state, L: Low modular state). Correlation coefficient is computed across all pairs of regions (black) and only with structurally connected pairs of regions (red). Results obtained from structural connectivity strengths without resampling are shown by broken lines for reference. Lower plots: mutual information of partitions between averaged structural connectivity and state centroids.

Moreover, similar trends were observed in structural connectivity strengths without resampling (Fig. 9B, plots with broken lines). These observations indicate that, on average, the more stereotypical functional connectivity patterns during periods of high modularity deviated more from the underlying brain structural networks, compared to functional connectivity patterns in the other states.

Discussion

In the present study, we investigated relationships between individual variations and dynamic fluctuations in the modularity of functional connectivity and examined connectivity patterns observed during periods of high and low modularity. Using multisession rs-fMRI data, we first confirmed that modularity measured over longer time scales displayed individual differences with moderate test-retest reliability (Fig. 3C). We then showed that, in individuals expressing high modularity in time-averaged analysis, time-resolved functional connectivity exhibited highly modular patterns more frequently (Figs. 5 and 6). During the high modular state, time-resolved functional connectivity exhibited higher similarity to each other, where its connectivity patterns were well characterized by the dissociation of

the DMN module from the DAN, VAN, SMN, and VIS modules (Fig. 7), and their average connectivity pattern was more dissimilar to the patterns in structural connectivity (Fig. 9B), compared to the low modular state. These results suggest that individual variability in long-time-scale modularity and dynamic fluctuations in short-time-scale modularity are closely interrelated and these fluctuations arise from the recurrence of functional connectivity patterns accompanied by increased DMN segregation and marked divergence from the background structural connectivity.

4.1. Test-retest reliability of modularity measures

Previous studies examined test-retest reliability of modularity in time-averaged analysis in a variety of data preprocessing conditions (Schwarz and McGonigle, 2011; Wang et al., 2011; Braun et al., 2012; Cao et al., 2014a). Scores similar to the ICC score in our study (0.45 across four runs) were also found in several conditions in each of these previous studies. Reliability of modularity measures derived from time-resolved analysis was first evaluated in this study. Reliability of mean time-resolved modularity (ICC = 0.42) and frequency of the high and low modular states (ICC = 0.28, 0.42) were fair to moderate, indicating somewhat stable individual variability across sessions and run in time-resolved modularity. In comparison to state frequency, the mean dwell time of a state was found to be less reliable (ICC: the high modular state, 0.11; the low modular state, 0.31), possibly due to a limited number of state transitions in each rs-fMRI run.

4.2. Individual variability and modularity fluctuations

We found that individual variations and dynamic fluctuations in modularity were closely interrelated. In individuals with higher/lower modularity in time-averaged analysis, mean time-resolved modularity was also high/low and frequency and mean dwell time of the high/low modular state were large, respectively (Fig. 5). This relationship can be interpreted in two ways. First, it can be seen to indicate that modularity in time-averaged analysis constrains the dynamics of time-resolved modularity. The notion that connectivity dynamics are constrained by their time-averaged properties was examined in recent dynamic functional connectivity studies (Thompson and Fransson, 2015; Betzel et al., 2016). The second interpretation is that individual variations in long-time-scale modularity arise from individual variations in short-time-scale modularity. The observation that the reliability of the modularity in time-averaged analysis and the frequency of the high and low modular states were comparable suggests that the magnitude of long-time-scale modularity originates from the heterogeneity in the dynamics of short-time-scale modularity. This implies that previous findings on relationships between modularity in time-averaged analysis and demographics

(Meunier et al., 2009a; Betzel et al., 2014; Cao et al., 2014b; Chan et al., 2014; Geerligs et al., 2015) or behavior (Bassett et al., 2011; Kitzbichler et al., 2011; Stevens et al., 2012) can be associated with individual differences in the dynamics of time-resolved modularity. This perspective is supported by recent studies demonstrating associations of the dynamics in connectivity patterns with demographics (Hutchison and Morton, 2015) and behavior (Barttfeld et al., 2015; Gonzalez-Castillo et al., 2015).

4.3. Connectivity patterns and modularity fluctuations

In the high modular state, connectivity patterns were similar to each other and were characterized by the recurrence of somewhat stereotypic patterns wherein the DMN module was decoupled from the attention and primary sensory modules. While in the low modular state, these modules tended to dissolve in dissimilar ways. The relatively stable modules during periods of high modularity contributed to form the modular state centroid within which overall absolute magnitude of functional connectivity was high (Fig. 7A). On the other hand, the many mutually dissimilar connectivity patterns during periods of low modularity resulted in the "flat" state centroid wherein the magnitude of functional connectivity was low due to the averaging of variable connectivity strengths (Fig. 7A). These two distinctive state centroids were also observed when connectivity states were detected using a *k*-means clustering algorithm (Fig. 8A), as in the prior literature (Allen et al., 2014; Damaraju et al., 2014; Barttfeld et al., 2015). This observation suggests that these characteristic spatiotemporal features of states did not depend on the precise manner by which connectivity states are detected or defined.

The present study does not allow firm conclusions about specific neurobiological mechanisms that underlie fluctuations in the modularity of functional connectivity. Nevertheless, our findings regarding the specific patterns of functional connectivity that underlie modularity fluctuations suggest a link to temporal changes in information segregation and integration across cortical networks (Sporns, 2013; Deco et al., 2015). During the high modular state, functional networks shared a common configuration of modules, with the DMN decoupled from the attention and primary sensory networks. This suggests that the high modular state corresponds to periods of increased segregation among task-positive and task-negative subsystems. In contrast, more variable connectivity patterns with less coherent modules were encountered during the low modular state. This state appears to be generally characterized by increased integration among functional subsystems, which collectively correspond to a large set of different connectivity patterns that may support efficient global communication across networks. In parallel, Shine and colleagues also reported that time-resolved functional connectivity exhibited transitions between states of segregated and integrated

network topology and that their state frequency was modulated by task demand and performance (Shine et al., 2016a) as well as attention and alertness (Shine et al., 2016b). Taken together, these findings suggest that fluctuations in the modularity of functional connectivity can be interpreted as a result of temporal changes in functional segregation and integration across whole-brain networks.

Another possibility is that fluctuations in the modularity of functional connectivity are not directly related to transient "moment-to-moment" cognitive processing but rather may reflect structured spatiotemporal patterns inherent in individual anatomical brain networks and relatively stable functional coupling strengths among networks of neuronal populations. As observed in oscillatory dynamics of a simple pendulum, a state point of a dynamical system fluctuates in a state space even when the system itself is time-invariant (Laumann et al., 2016). For connectivity dynamics, Zalesky et al. (2014) demonstrated that a model simulating neuronal population dynamics, consisting of neural mass models interconnected according to macaque axonal connectivity with time-invariant coupling parameters (Honey et al., 2007), can generate characteristic time-varying functional connectivity patterns exhibiting fluctuations in efficiency of networks, which is indeed closely related to modularity of networks. In another cortical dynamics model, consisting of the Kuramoto oscillators coupled based on structural connectivity and time-invariant coupling parameters, fluctuations in the global synchrony degree (metastable synchronization; Shanahan et al., 2010) emerge when parameters in this model are fitted to reproduce empirical functional connectivity (Cabral et al., 2011). Based on these prior findings, fluctuations in the modularity of functional connectivity may be interpreted as a manifestation of self-organized cortical dynamics emergent from dynamic process that unfold on a relatively stable backbone of structural connectivity.

4.4. Relations to structural connectivity

The state centroid during high modularity periods exhibited lower and the centroid during low modularity periods exhibited higher similarity to structural connectivity, respectively (Fig. 9B). This finding is in line with earlier results in the macaque brain (Barttfeld et al., 2015), which demonstrated that more/less modular cluster centroids were less/more similar to structural connectivity derived from tract tracing studies. Similarly, Liégeois et al. (2016) showed that functional networks during periods of low similarity to structural networks exhibited a canonical modular network topology where the default mode and primary sensory networks were clearly dissociated from each other. Liégeois et al. associated this state with low modularity—this inconsistency with our findings likely results from their

use of absolute functional connectivity for computing the modularity score, which underestimates modularity when a large number of between-module connections have strong negative weights.

From these observations on the relations to structural connectivity, fluctuations of wakefulness and drowsiness are emerged as another possible interpretation for the fluctuations of high and low modularity. Tagliazucchi et al. (2015) reported that similarity between functional and structural connectivity increases during deep sleep. Barttfeld et al. (2015) showed that connectivity states of which centroid has greater similarity to structural connectivity are detected more frequently in moderate and deep sedation conditions than in an awake condition. Furthermore, Laumann et al. (2016) pointed out that drowsiness is one of the factors causing the temporal variability in functional connectivity. Therefore, the low modular state with higher similarity to structural connectivity may correspond to drowsiness and the high modular state to wakefulness. With this assumption, the decrease of within-connectivity strength in DMN in the low modular state centroid (Fig. 7A) is consistent with previous findings on the breakdown of the DMN module during deep sleep (Horovitz et al., 2009). Significant divergence of the functional connectivity patterns from the underlying structural connectivity in the high modular state can be attributed to increased participation of indirect structural paths in neuronal communication during wakefulness.

4.5. Limitations

Several issues on methodological limitations have to be taken into account when interpreting the results. First, subject head movements are potential confounds in rs-fMRI data (Power et al., 2012). In our case, subject motion may affect characterization of modularity fluctuations. To solve this issue, we excluded high motion subjects, interpolated spikes in the BOLD time series, and regressed out motion time series. Although it remains difficult to completely exclude motion effects, modularity measures were significantly correlated with mean framewise displacement in only a subset of rs-fMRI runs and therefore our findings cannot be fully attributed to motion artifacts. Second, while a sliding window approach is a simple and the most commonly used method for estimating time-resolved functional connectivity (Hutchison et al., 2013a), this method has limitations especially in detecting sharp connectivity transitions (Lindquist et al. 2014; Shine et al., 2015; Shakil et al., 2016). We used a window length longer than the reciprocal of low cutoff frequency to suppress spurious connectivity dynamics (Leonardi and Van De Ville, 2015; Zalesky and Breakspear, 2015) though it may decrease temporal sensitivity. This highlights the need to establish methods that can handle connectivity dynamics on multiple time scales. Third, modularity maximization has a shortcoming in detecting modules below a certain scale under certain conditions (the resolution limit; Fortunato and

Barthelemy, 2007). We used a single (default) resolution parameter to properly compare the modularity quality function across subjects and time samples. However, this prevents the algorithm from detecting modules of different sizes. A possible strategy to circumvent this issue is to explore a range of resolution parameters in each analysis to reveal multiscale modules in networks (Betz et al., 2013).

Another limitation comes from the data processing steps independently applied to the NKI and HCP datasets. The use of multiple datasets with their own data processing pipeline was helpful for finding observations independent to manners of data acquisition and processing. However, with the current approach, one cannot determine which factor (data acquisition, parcellation scheme or window parameters, etc.) was responsible for the discrepancies in the results between the two datasets. While in this study we have primarily focused on the results commonly obtained from the NKI and HCP datasets, there were several discrepancies in the results. For instance, the dissociation of the DMN module from the DAN and VAN modules in the high modular state centroid was more pronounced in the NKI dataset (Fig. 7A) and the overall similarity to structural connectivity in the state centroids was greater in the HCP dataset (Fig. 9B). Factors causing such discrepancies may be uncovered by applying multiple combinations of data processing steps to both datasets.

4.6. Future directions

Our study demonstrated characteristic dynamic connectivity patterns during high and low modularity periods and established that these fluctuations are linked to individual differences in modularity expressed on longer time scales. Important topics for future research are further investigating fluctuations in the modularity of functional connectivity to explore their functional meaning and structural substrates. Potential roles of modularity fluctuations in function and behavior can be explored by relating modularity fluctuations to demographic and behavioral data across individuals. Investigating structural features predictive of the dynamics of modularity may reveal an anatomical basis of modularity fluctuations, including the causes for higher/lower similarity to structural connectivity in the low/high modular state. In addition, analyzing fluctuations in the modularity using whole-brain computational models that can simulate switching behavior of functional connectivity (e.g. Hansen et al., 2015) may allow investigating the mechanistic origin of modularity fluctuations and their individual variability. Future studies are needed to provide a more comprehensive understanding of fluctuations in the modularity of functional connectivity.

5. Conclusions

While modularity of human cortical functional networks was shown to vary between and within individuals, little is known about within-individual dynamic fluctuations in short-time-scale modularity and their relation to between-individual variability in long-time-scale modularity. Here, we have characterized dynamic modularity fluctuations by relating them to individual variability in modularity in a conventional time-averaged analysis and examining connectivity patterns during periods of high and low time-resolved modularity. After confirming moderate test-retest reliability in modularity measured over longer time scales, we found that time-resolved functional networks exhibited highly modular connectivity patterns more frequently in subjects expressing high modularity in time-averaged analysis. Connectivity patterns during high modularity periods were well characterized by a dissociation of task-positive and task-negative systems, exhibiting greater similarity to each other compared to low modularity periods, and connectivity patterns averaged within high modularity periods less reflected connectivity patterns observed in the underlying structural cortical networks. Altogether, these results suggest that individual variations and dynamic fluctuations in modularity are interrelated, wherein fluctuations of modularity emerge from the recurrence of stereotypic functional connectivity patterns accompanied by a shift away from their background structural connectivity. These findings provide new insights into individual variability in modular organization of human cortical functional networks from a time-varying network perspective.

Acknowledgements

M.F. was supported by a Uehara Memorial Foundation Postdoctoral Fellowship and a Japan Society for the Promotion of Science Postdoctoral Fellowship for Research Abroad. O.S. was supported by the J.S. McDonnell Foundation (22002082) and the National Institutes of Health (R01 AT009036-01). R.F.B. was supported by the National Science Foundation/Integrative Graduate Education and Research Traineeship Training Program in the Dynamics of Brain-Body-Environment Systems at Indiana University (0903495). X.N.Z was supported by the National Key Basic Research and Development Program (973 Program; 2015CB351702) and the Natural Sciences Foundation of China (81471740, 81220108014). X.N.Z. and O.S. are members of an international collaboration team (trial stage) supported by the CAS K.C. Wong Education Foundation. Data were provided in part by the Human Connectome Project, WU-Minn Consortium (Principal Investigators: David Van Essen and Kamil Ugurbil; 1U54MH091657) funded by the 16 NIH Institutes and Centers that support the NIH Blueprint for Neuroscience Research; and by the McDonnell Center for Systems Neuroscience at Washington University.

References

- Allen, E.A., Damaraju, E., Plis, S.M., Erhardt, E.B., Eichele, T., Calhoun, V.D., 2014. Tracking whole-brain connectivity dynamics in the resting state. *Cereb. Cortex* 24, 663–676.
- Andellini, M., Cannatà, V., Gazzellini, S., Bernardi, B., Napolitano, A., 2015. Test-retest reliability of graph metrics of resting state MRI functional brain networks: a review. *J. Neurosci. Methods* 253, 183–192.
- Ashburner, J., 2012. SPM: a history. *NeuroImage* 62, 791–800.
- Barttfeld, P., Uhrig, L., Sitt, J.D., Sigman, M., Jarraya, B., Dehaene, S., 2015. Signature of consciousness in the dynamics of resting-state brain activity. *Proc. Natl. Acad. Sci. U. S. A.* 112, 887–892.
- Bassett, D.S., Wymbs, N.F., Porter, M.A., Mucha, P.J., Carlson, J.M., Grafton, S.T., 2011. Dynamic reconfiguration of human brain networks during learning. *Proc. Natl. Acad. Sci. U. S. A.* 108, 7641–7646.
- Betzel, R.F., Byrge, L., He, Y., Goñi, J., Zuo, X.N., Sporns, O., 2014. Changes in structural and functional connectivity among resting-state networks across the human lifespan. *NeuroImage* 102, 345–357.
- Betzel, R.F., Fukushima, M., He, Y., Zuo, X.N., Sporns, O., 2016. Dynamic fluctuations coincide with periods of high and low modularity in resting-state functional brain networks. *NeuroImage* 127, 287–297.
- Betzel, R.F., Griffà, A., Avena-Koenigsberger, A., Goñi, J., Thiran, J.P., Hagmann, P., Sporns, O., 2013. Multi-scale community organization of the human structural connectome and its relationship with resting-state functional connectivity. *Netw. Sci.* 1, 353–373.
- Braun, U., Plichta, M.M., Esslinger, C., Sauer, C., Haddad, L., Grimm, O., Mier, D., Mohnke, S., Heinz, A., Erk, S., Walter, H., Seiferth, N., Kirsch, P., Meyer-Lindenberg, A., 2012. Test-retest reliability of resting-state connectivity network characteristics using fMRI and graph theoretical measures. *NeuroImage* 59, 1404–1412.
- Bullmore, E.T., Sporns, O., 2012. The economy of brain network organization. *Nat. Rev. Neurosci.* 13, 336–349.
- Cabral, J., Hugues, E., Sporns, O., Deco, G., 2011. Role of local network oscillations in resting-state functional connectivity. *NeuroImage* 57, 130–139.

- Calhoun, V.D., Miller, R., Pearlson, G., Adali, T., 2014. The chronnectome: time-varying connectivity networks as the next frontier in fMRI data discovery. *Neuron* 84, 262–274.
- Cammoun, L., Gigandet, X., Meskaldji, D., Thiran, J.P., Sporns, O., Do, K.Q., Maeder, P., Meuli, R., Hagmann, P., 2012. Mapping the human connectome at multiple scales with diffusion spectrum MRI. *J. Neurosci. Methods* 203, 386–397.
- Cao, H., Plichta, M.M., Schäfer, A., Haddad, L., Grimm, O., Schneider, M., Esslinger, C., Kirsch, P., Meyer-Lindenberg, A., Tost, H., 2014a. Test-retest reliability of fMRI-based graph theoretical properties during working memory, emotion processing, and resting state. *NeuroImage* 84, 888–900.
- Cao, M., Wang, J.H., Dai, Z.J., Cao, X.Y., Jiang, L.L., Fan, F.M., Song, X.W., Xia, M.R., Shu, N., Dong, Q., Milham, M.P., Castellanos, F.X., Zuo, X.N., He, Y., 2014b. Topological organization of the human brain functional connectome across the lifespan. *Dev. Cogn. Neurosci.* 7, 76–93.
- Chan, M.Y., Park, D.C., Savalia, N.K., Petersen, S.E., Wig, G.S., 2014. Decreased segregation of brain systems across the healthy adult lifespan. *Proc. Natl. Acad. Sci. U. S. A.* 111, E4997–E5006.
- Chang, C., Glover, G.H., 2010. Time-frequency dynamics of resting-state brain connectivity measured with fMRI. *NeuroImage* 50, 81–98.
- Chen, T., Cai, W., Ryali, S., Supekar, K., Menon, V., 2016. Distinct global brain dynamics and spatiotemporal organization of the salience network. *PLoS Biol.* 14, e1002469.
- Clune, J., Mouret, J.B., Lipson, H., 2013. The evolutionary origins of modularity. *Proc. Biol. Sci.* 280, 20122863.
- Cox, R.W., 2012. AFNI: what a long strange trip it's been. *NeuroImage* 62, 743–747.
- Damaraju, E., Allen, E.A., Belger, A., Ford, J.M., McEwen, S., Mathalon, D.H., Mueller, B.A., Pearlson, G.D., Potkin, S.G., Preda, A., Turner, J.A., Vaidya, J.G., van Erp, T.G., Calhoun, V.D., 2014. Dynamic functional connectivity analysis reveals transient states of dysconnectivity in schizophrenia. *NeuroImage Clin* 5, 298–308.
- Deco, G., Tononi, G., Boly, M., Kringelbach, M.L., 2015. Rethinking segregation and integration: contributions of whole-brain modelling. *Nat. Rev. Neurosci.* 16, 430–439.

de Reus, M.A., van den Heuvel, M.P., 2013. Rich club organization and intermodule communication in the cat connectome. *J Neurosci* 33, 12929–12939.

de Reus, M.A., van den Heuvel, M.P., 2014. Simulated rich club lesioning in brain networks: a scaffold for communication and integration? *Front Hum Neurosci* 8, 647.

Felleman, D.J., Van Essen, D.C., 1991. Distributed hierarchical processing in the primate cerebral cortex. *Cereb. Cortex* 1, 1–47.

Fischl, B., 2012. FreeSurfer. *NeuroImage* 62, 774–781.

Fortunato, S., Barthelemy, M., 2007. Resolution limit in community detection. *Proc. Natl. Acad. Sci. U. S. A.* 104, 36–41.

Friston, K.J., Williams, S., Howard, R., Frackowiak, R.S., Turner, R., 1996. Movement-related effects in fMRI time-series. *Magn. Reson. Med.* 35, 346–355.

Geerligs, L., Renken, R.J., Saliassi, E., Maurits, N.M., Lorist, M.M., 2015. A brain-wide study of age-related changes in functional connectivity. *Cereb. Cortex* 25, 1987–1999.

Glasser, M.F., Sotiropoulos, S.N., Wilson, J.A., Coalson, T.S., Fischl, B., Andersson, J.L., Xu, J., Jbabdi, S., Webster, M., Polimeni, J.R., Van Essen, D.C., Jenkinson M for the WU-Minn HCP Consortium, 2013. The minimal preprocessing pipelines for the Human Connectome Project. *NeuroImage* 80, 105–124.

Gonzalez-Castillo, J., Handwerker, D.A., Robinson, M.E., Hoy, C.W., Buchanan, L.C., Saad, Z.S., Bandettini, P.A., 2014. The spatial structure of resting state connectivity stability on the scale of minutes. *Front. Neurosci.* 8, 138.

Gonzalez-Castillo, J., Hoy, C.W., Handwerker, D.A., Robinson, M.E., Buchanan, L.C., Saad, Z.S., Bandettini, P.A., 2015. Tracking ongoing cognition in individuals using brief, whole-brain functional connectivity patterns. *Proc. Natl. Acad. Sci. U. S. A.* 112, 8762–8767.

Good, B.H., de Montjoye, Y.A., Clauset, A., 2010. Performance of modularity maximization in practical contexts. *Phys. Rev. E* 81, 046106.

- Guo, C.C., Kurth, F., Zhou, J., Mayer, E.A., Eickhoff, S.B., Kramer, J.H., Seeley, W.W., 2012. One-year test-retest reliability of intrinsic connectivity network fMRI in older adults. *NeuroImage* 61, 1471–1483.
- Hagmann, P., Cammoun, L., Gigandet, X., Meuli, R., Honey, C.J., Wedeen, V.J., Sporns, O., 2008. Mapping the structural core of human cerebral cortex. *PLoS Biol.* 6, e159.
- Hagmann, P., Kurant, M., Gigandet, X., Thiran, P., Wedeen, V.J., Meuli, R., Thiran, J.P., 2007. Mapping human whole-brain structural networks with diffusion MRI. *PLoS One* 2, e597.
- Handwerker, D.A., Roopchansingh, V., Gonzalez-Castillo, J., Bandettini, P.A., 2012. Periodic changes in fMRI connectivity. *NeuroImage* 63, 1712–1719.
- Hansen, E.C.A., Battaglia, D., Spiegler, A., Deco, G., Jirsa, V.K., 2015. Functional connectivity dynamics: modeling the switching behavior of the resting state. *NeuroImage* 105, 525–535.
- Harriger, L., van den Heuvel, M.P., Sporns, O., 2012. Rich club organization of macaque cerebral cortex and its role in network communication. *PLoS One* 7, e46497.
- Hilgetag, C.C., Burns, G.A., O’Neill, M.A., Scannell, J.W., Young, M.P., 2000. Anatomical connectivity defines the organization of clusters of cortical areas in the macaque monkey and the cat. *Philos. Trans. R. Soc. Lond. B Biol. Sci.* 355, 91–110.
- Honey, C.J., Kötter, R., Breakspear, M., Sporns, O., 2007. Network structure of cerebral cortex shapes functional connectivity on multiple time scales. *Proc. Natl. Acad. Sci. U. S. A.* 104, 10240–10245.
- Honey, C.J., Sporns, O., Cammoun, L., Gigandet, X., Thiran, J.P., Meuli, R., Hagmann, P., 2009. Predicting human resting-state functional connectivity from structural connectivity. *Proc. Natl. Acad. Sci. U. S. A.* 106, 2035–2040.
- Horowitz, S.G., Braun, A.R., Carr, W.S., Picchioni, D., Balkin, T.J., Fukunaga, M., Duyn, J.H., 2009. Decoupling of the brain’s default mode network during deep sleep. *Proc. Natl. Acad. Sci. U. S. A.* 106, 11376–11381.
- Hutchison, R.M., Morton, J.B., 2015. Tracking the brain’s functional coupling dynamics over development. *J. Neurosci.* 35, 6849–6859.

Hutchison, R.M., Womelsdorf, T., Allen, E.A., Bandettini, P.A., Calhoun, V.D., Corbetta, M., Della Penna, S., Duyn, J.H., Glover, G.H., Gonzalez-Castillo, J., Handwerker, D.A., Keilholz, S., Kiviniemi, V., Leopold, D.A., de Pasquale, F., Sporns, O., Walter, M., Chang, C., 2013a. Dynamic functional connectivity: promise, issues, and interpretations. *NeuroImage* 80, 360–378.

Hutchison, R.M., Womelsdorf, T., Gati, J.S., Everling, S., Menon, R.S., 2013b. Resting-state networks show dynamic functional connectivity in awake humans and anesthetized macaques. *Hum. Brain Mapp.* 34, 2154–2177.

Jarrell, T.A., Wang, Y., Bloniarz, A.E., Brittin, C.A., Xu, M., Thomson, J.N., Albertson, D.G., Hall, D.H., Emmons, S.W., 2012. The connectome of a decision-making neural network. *Science* 337, 437–444.

Jenkinson, M., Beckmann, C.F., Behrens, T.E.J., Woolrich, M.W., Smith, S.M., 2012. FSL. *NeuroImage* 62, 782–790.

Jones, D.T., Vemuri, P., Murphy, M.C., Gunter, J.L., Senjem, M.L., Machulda, M.M., Przybelski, S.A., Gregg, B.E., Kantarci, K., Knopman, D.S., Boeve, B.F., Petersen, R.C., Jack, C.R., 2012. Non-stationarity in the "resting brain's" modular architecture. *PLoS One* 7, e39731.

Kashtan, N., Alon, U., 2005. Spontaneous evolution of modularity and network motifs. *Proc. Natl. Acad. Sci. U. S. A.* 102, 13773–13778.

Kashtan, N., Noor, E., Alon, U., 2007. Varying environments can speed up evolution. *Proc. Natl. Acad. Sci. U. S. A.* 104, 13711–13716.

Kitzbichler, M.G., Henson, R.N.A., Smith, M.L., Nathan, P.J., Bullmore, E.T., 2011. Cognitive effort drives workspace configuration of human brain functional networks. *J. Neurosci.* 31, 8259–8270.

Laumann, T.O., Snyder, A.Z., Mitra, A.M., Gordon, E.M., Gratton, C., Adeyemo, B., Gilmore, A.W., Nelson, S.M., Berg, J.J., Greene, D.J., McCarthy, J.E., Tagliazucchi, E., Laufs, H., Schlaggar, B.L., Dosenbach, N.U.F., Petersen, S.E., 2016. On the stability of BOLD fMRI correlations. *Cereb. Cortex*, to appear.

Leonardi, N., Richiardi, J., Gschwind, M., Simioni, S., Annoni, J.M., Schluep, M., Vuilleumier, P., Van De Ville, D., 2013. Principal components of functional connectivity: a new approach to study dynamic brain connectivity during rest. *NeuroImage* 83, 937–950.

Leonardi, N., Van De Ville, D., 2015. On spurious and real fluctuations of dynamic functional connectivity during rest. *NeuroImage* 104, 430–436.

Liégeois, R., Ziegler, E., Phillips, C., Geurts, P., Gómez, F., Bahri, M.A., Yeo, B.T.T., Soddu, A., Vanhauzenhuysse, A., Laureys, S., Sepulchre, R., 2016. Cerebral functional connectivity periodically (de)synchronizes with anatomical constraints. *Brain Struct. Func.* 221, 2985–2997.

Lindquist, M.A., Xu, Y., Nebel, M.B., Caffo, B.S., 2014. Evaluating dynamic bivariate correlations in resting-state fMRI: a comparison study and a new approach. *NeuroImage* 101, 531–546.

McGraw, K.O., Wong, S.P., 1996. Forming inferences about some intraclass correlation coefficients. *Psychol. Methods* 1, 30–46.

Meunier, D., Achard, S., Morcom, A., Bullmore, E.T., 2009a. Age-related changes in modular organization of human brain functional networks. *NeuroImage* 44, 715–723.

Meunier, D., Lambiotte, R., Fornito, A., Ersche, K.D., Bullmore, E.T., 2009b. Hierarchical modularity in human brain functional networks. *Front. Hum. Neurosci.* 3, 37.

Mori, S., Crain, B.J., Chacko, V.P., Van Zijl, P.C.M., 1999. Three-dimensional tracking of axonal projections in the brain by magnetic resonance imaging. *Ann. Neurol.* 45, 265–269.

Müller, R., Büttner, P., 1994. A critical discussion of intraclass correlation coefficients. *Stat. Med.* 13, 2465–2476.

Newman, M.E.J., Girvan, M., 2004. Finding and evaluating community structure in networks. *Phys. Rev. E* 69, 026113.

Nooner, K.B., Colcombe, S.J., Tobe, R.H., Mennes, M., Benedict, M.M., Moreno, A.L., Panek, L.J., Brown, S., Zavitz, S.T., Li, Q., Sikka, S., Gutman, D., Bangaru, S., Schlachter, R.T., Kamiel, S.M., Anwar, A.R., Hinz, C.M., Kaplan, M.S., Rachlin, A.B., Adelsberg, S., Cheung, B., Khanuja, R., Yan, C., Craddock, C.C., Calhoun, V.,

Courtney, W., King, M., Wood, D., Cox, C.L., Kelly, A.M.C., Di Martino, A., Petkova, E., Reiss, P.T., Duan, N., Thomsen, D., Biswal, B., Coffey, B., Hoptman, M.J., Javitt, D.C., Pomara, N., Sidtis, J.J., Koplewicz, H.S., Castellanos, F.X., Leventhal, B.L., Milham, M.P., 2012. The NKI-Rockland sample: a model for accelerating the pace of discovery science in psychiatry. *Front. Neurosci.* 6, 152.

Power, J.D., Barnes, K.A., Snyder, A.Z., Schlaggar, B.L., Petersen, S.E., 2012. Spurious but systematic correlations in functional connectivity MRI networks arise from subject motion. *NeuroImage* 59, 2142–2154.

Power, J.D., Cohen, A.L., Nelson, S.M., Wig, G.S., Barnes, K.A., Church, J.A., Vogel, A.C., Laumann, T.O., Miezin, F.M., Schlaggar, B.L., Petersen, S.E., 2011. Functional network organization of the human brain. *Neuron* 72, 665–678.

Prichard, D., Theiler, J., 1994. Generating surrogate data for time series with several simultaneously measured variables. *Phys. Rev. Lett.* 73, 951–954.

Rousson, V., Gasser, T., Seifert, B., 2002. Assessing intrarater, interrater and test-retest reliability of continuous measurements. *Stat. Med.* 21, 3431–3446.

Rubinov, M., Sporns, O., 2011. Weight-conserving characterization of complex functional brain networks. *NeuroImage* 56, 2068–2079.

Scannell, J.W., Blakemore, C., Young, M.P., 1995. Analysis of connectivity in the cat cerebral cortex. *J. Neurosci.* 15, 1463–1483.

Schwarz, A.J., McGonigle, J., 2011. Negative edges and soft thresholding in complex network analysis of resting state functional connectivity data. *NeuroImage* 55, 1132–1146.

Shakil, S., Lee, C.H., Keilholz, S.D., 2016. Evaluation of sliding window correlation performance for characterizing dynamic functional connectivity and brain states. *NeuroImage* 133, 111–128.

Shanahan, M., 2010. Metastable chimera states in community-structured oscillator networks. *Chaos* 20, 013108.

Shen, K., Bezgin, G., Hutchison, R.M., Gati, J.S., Menon, R.S., Everling, S., McIntosh, A.R., 2012. Information processing architecture of functionally defined clusters in the macaque cortex. *J. Neurosci.* 32, 17465–17476.

- Shen, K., Hutchison, R.M., Bezgin, G., Everling, S., McIntosh, A.R., 2015. Network structure shapes spontaneous functional connectivity dynamics. *J. Neurosci.* 35, 5579–5588.
- Shine, J.M., Bell, P.T., Koyejo, O., Bissett, P.G., Gorgolewski, K.J., Moodie, C.A., Poldrack, R.A., 2016a. Dynamic fluctuations in global brain network topology characterize functional states during rest and behavior. arXiv 1511.02976 [q-bio.NC].
- Shine, J.M., Koyejo, O., Bell, P.T., Gorgolewski, K.J., Gilat, M., Poldrack, R.A., 2015. Estimation of dynamic functional connectivity using Multiplication of Temporal Derivatives. *NeuroImage* 122, 399–407.
- Shine, J.M., Koyejo, O., Poldrack, R.A., 2016b. Temporal metastates are associated with differential patterns of time-resolved connectivity, network topology, and attention. *Proc. Natl. Acad. Sci. U. S. A.*, doi:10.1073/pnas.1604898113.
- Shrout, P.E., Fleiss, J.L., 1979. Intraclass correlations: uses in assessing rater reliability. *Psychol. Bull.* 86, 420–428.
- Sporns, O., 2013. Network attributes for segregation and integration in the human brain. *Curr. Opin. Neurobiol.* 23, 162–171.
- Sporns, O., Betzel, R.F., 2016. Modular brain networks. *Annu. Rev. Psychol.* 67, 613–640.
- Stevens, A.A., Tappon, S.C., Garg, A., Fair, D.A., 2012. Functional brain network modularity captures inter- and intra-individual variation in working memory capacity. *PLoS One* 7, e30468.
- Tagliazucchi, E., Crossley, N., Bullmore, E.T., Laufs, H., 2015. Deep sleep divides the cortex into opposite modes of anatomical functional coupling. *Brain Struct. Func.*, doi:10.1007/s00429-015-1162-0.
- Thompson, W.H., Fransson, P., 2015. The mean-variance relationship reveals two possible strategies for dynamic brain connectivity analysis in fMRI. *Front. Hum. Neurosci.* 9, 398.
- Towilson, E.K., Vértes, P.E., Ahnert, S.E., Schafer, W.R., Bullmore, E.T., 2013. The rich club of the *C. elegans* neuronal connectome. *J. Neurosci.* 33, 6380–6387.

van den Heuvel, M.P., Scholtens, L.H., de Reus, M.A., Kahn, R.S., 2016. Associated microscale spine density and macroscale connectivity disruptions in schizophrenia. *Biol. Psychiatry* 80, 293–301.

van den Heuvel, M.P., Scholtens, L.H., Feldman Barrett, L., Hilgetag, C.C., de Reus, M.A., 2015. Bridging cytoarchitectonics and connectomics in human cerebral cortex. *J. Neurosci.* 35, 13943–13948.

van den Heuvel, M.P., Sporns, O., 2011. Rich-club organization of the human connectome. *J. Neurosci.* 31, 15775–15786.

van den Heuvel, M.P., Sporns, O., 2013. An anatomical substrate for integration among functional networks in human cortex. *J. Neurosci.* 33, 14489–14500.

Van Essen, D.C., Smith, S.M., Barch, D.M., Behrens, T.E.J., Yacoub, E., Ugurbil K for the WU-Minn HCP Consortium, 2013. The WU-Minn Human Connectome Project: an overview. *NeuroImage* 80, 62–79.

Wang, J.H., Zuo, X.N., Gohel, S., Milham, M.P., Biswal, B.B., He, Y., 2011. Graph theoretical analysis of functional brain networks: test-retest evaluation on short- and long-term resting-state functional MRI data. *PLoS One* 6, e21976.

Wang, R., Benner, T., Sorensen, A.G., Wedeen, V.J., 2007. Diffusion Toolkit: a software package for diffusion imaging data processing and tractography. *Proc. Int. Soc. Magn. Reson. Med.* 15, 3720.

White, J.G., Southgate, E., Thomson, J.N., Brenner, S., 1986. The structure of the nervous system of the nematode *Caenorhabditis elegans*. *Philos. Trans. R. Soc. Lond. B Biol. Sci.* 314, 1–340.

Xu, T., Yang, Z., Jiang, L., Xing, X.X., Zuo, X.N., 2015. A Connectome Computation System for discovery science of brain. *Sci. Bull.* 60, 86–95.

Yeh, F.C., Wedeen, V.J., Tseng, W.Y.I., 2010. Generalized q-sampling imaging. *IEEE Trans. Med. Imaging* 29, 1626–1635.

Yeo, B.T.T., Krienen, F.M., Sepulcre, J., Sabuncu, M.R., Lashkari, D., Hollinshead, M., Roffman, J.L., Smoller, J.W., Zollei, L., Polimeni, J.R., Fischl, B., Liu, H., Buckner, R.L., 2011. The organization of the human cerebral cortex estimated by intrinsic functional connectivity. *J. Neurophysiol.* 106, 1125–1165.

- Yu, S., Huang, D., Singer, W., Nikolić, D., 2008. A small world of neuronal synchrony. *Cereb. Cortex* 18, 2891–2901.
- Zalesky, A., Breakspear, M., 2015. Towards a statistical test for functional connectivity dynamics. *NeuroImage* 114, 466–470.
- Zalesky, A., Fornito, A., Cocchi, L., Gollo, L.L., Breakspear, M., 2014. Time-resolved resting-state brain networks. *Proc. Natl. Acad. Sci. U. S. A.* 111, 10341–10346.
- Zamora-López, G., Zhou, C., Kurths, J., 2010. Cortical hubs form a module for multisensory integration on top of the hierarchy of cortical networks. *Front. Neuroinform.* 4, 1.
- Zhang, J., Cheng, W., Liu, Z., Zhang, K., Lei, X., Yao, Y., Becker, B., Liu, Y., Kendrick, K.M., Lu, G., Feng, J., 2016. Neural, electrophysiological and anatomical basis of brain-network variability and its characteristic changes in mental disorders. *Brain* 139, 2307–2321.
- Zuo, X.N., Xing, X.X., 2014. Test-retest reliabilities of resting-state fMRI measurements in human brain functional connectomics: a systems neuroscience perspective. *Neurosci. Biobehav. Rev.* 45, 100–118.